ACS OMEGA

Open Access

http://pubs.acs.org/journal/acsodf

Article

Microwave-Assisted Synthesis of Functionalized Carbon Nanospheres Using Banana Peels: pH-Dependent Synthesis, Characterization, and Selective Sensing Applications

Tavishi Chopra and Raman Parkesh*

Cite This: *ACS Omega* 2024, 9, 4555−4571

Read Online

ACCESS | Metrics & More | Article Recommendations | Supporting Information

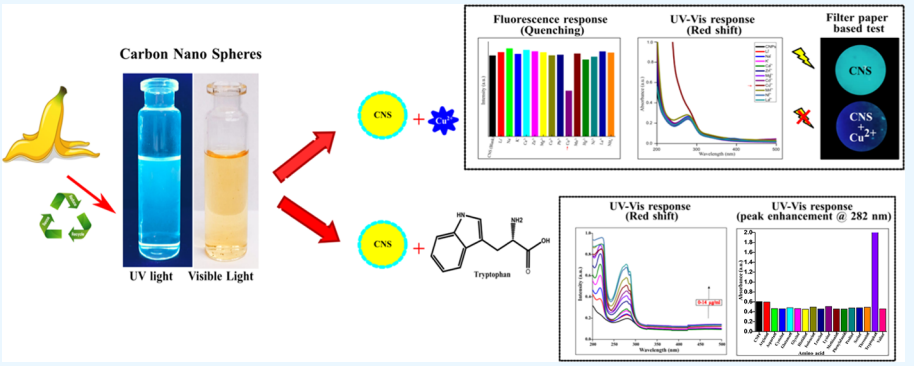

ABSTRACT: This work presents a microwave-based green synthesis method for producing carbon nanospheres (CNSs) and investigates the impact of presynthesis pH on their size and assembly. The resulting CNSs are monodispersed, averaging 35 nm in size, and exhibit notable characteristics including high water solubility, photostability, and a narrow size distribution, achieved within a synthesis time of 15 min. The synthesized CNS features functional groups such as −OH, −COOH, −NH, −C−O−C, ═C−H, and −CH. This diversity empowers the CNS for various applications including sensing. The CNS exhibits a distinct UV peak at 282 nm and emits intense fluorescence at 430 nm upon excitation at 350 nm. These functionalized CNSs enable selective and specific sensing of Cu^{2+} ions and the amino acid tryptophan (Trp) in aqueous solutions. In the presence of Cu^{2+} ions, static-based quenching of CNS fluorescence was observed due to the chelation-enhanced quenching (CHEQ) effect. Notably, Cu^{2+} ions induce a substantial change in UV spectra alongside a red-shift in the peak position. The limits of detection and quantification for Cu^{2+} ions with CNS are determined as 0.73 and 2.45 μg/mL, respectively. Additionally, on interaction with tryptophan, the UV spectra of CNS display a marked increase in the peak at 282 nm, accompanied by a red-shift phenomenon. The limits of detection and quantification for L-tryptophan are 4.510×10^{-3} and 1.50×10^{-2} μg/mL, respectively, indicating its significant potential for biological applications. Furthermore, the practical applicability of CNSs is demonstrated by their successful implementation in analyzing real water samples and filter paper-based examination, showcasing their effectiveness for on-site sensing.

1. INTRODUCTION

Bananas, scientifically known as *Musa sapientum*, rank among the most widely cultivated tropical fruit crops globally. However, a significant portion of these fruits goes to waste after consumption, contributing to a substantial environmental burden. Worldwide banana waste production amounts to a staggering 114.08 million metric tons, leading to various environmental challenges, including global warming, soil degradation, and water pollution.[1] Banana waste is rich in valuable resources, including cellulose, hemicelluloses, calcium, magnesium, and natural fibers. These components hold immense industrial potential, spanning applications such as bioplastic production, fermentation, fertilizer manufacturing, biofuel generation, and agricultural applications.[2−6] Additionally, a considerable quantity of banana peels is discarded as waste, primarily composed of carbohydrates that can be harnessed for nanoparticle production.

Nanoparticles these days have garnered significant attention due to their versatile applications, including medical diagnostics, fluorescent sensing, catalytic degradation, bioimaging, labeling, metal sensing, biosensing, filtration, water treatment, and drug delivery.[7−10] There is a complete alteration of an element when it comes in the nano range,

Received: September 29, 2023
Revised: December 15, 2023
Accepted: December 22, 2023
Published: January 16, 2024

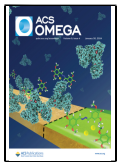

for example, C60, which is chemically inert makes very reactive bonds due to their enhanced reactions making CNS a competent entity for various applications.[11] The conventional synthesis of nanoparticles typically involves time-consuming hydrothermal reactions, requiring hours to days for completion. Efforts have been made to streamline nanoparticle synthesis, reduce production time, and incorporate functional appendages using minimal external agents, making it cost-effective for industrial-scale production. Additionally, in recent years, there has been a growing interest in detecting heavy metals, such as copper (Cu^{2+}), in ecological and biological contexts due to their adverse environmental impact. Cu^{2+} is one of the most abundant metals in the human body and plays essential roles in various physiological processes, including cell signaling, oxygen transport, energy generation, and neural functioning. However, elevated levels of copper in the environment can lead to health issues and diseases, necessitating strict implementation of regulatory limits, such as the EPA's permissible Cu^{2+} quantity of 1.3 ppm (20 μM).[12−14] Due to specific appendages on the surface of nanoparticles, they are also investigated to sense amino acids as they are the building block of proteins, and their levels can directly impact the structure and assembly of proteins formed in the body. For example, tryptophan (Trp) is involved in inhibiting various enzymes indulged in the biosynthesis of β-amyloid and this protein is directly involved in Alzheimer's disease,[15−19] Trp has a significant contribution in delaying aging and also in aging-related protein decline. Additionally, the nanoparticle sensor became a potential embodiment to sense the Trp amino acid. Trp is a critical amino acid involved in various metabolic activities, including sleep regulation, neurotransmitter synthesis, and mood regulation. Detecting Trp within specific concentration ranges is essential for maintaining nitrogen balance and has relevance in health research and disease diagnosis.[20−26]

This study focuses on the eco-friendly synthesis of carbon nanospheres (CNSs) using banana peels as a sustainable precursor. CNSs, spherical carbon nanoparticles ranging from 1 to 100 nm in size, are the focus of this research, which aims to rapidly synthesize them from banana peels and explore their potential applications. Notably, this research marks a novel attempt to achieve the swift synthesis of CNSs from banana peels in just 15 min, with a specific emphasis on their utility in detecting Cu^{2+} and Trp. Our studies introduce a green one-step synthesis method, optimizing temperature, pressure, hold time, and cooling conditions for cost-effective, eco-friendly, and prefunctionalized nanoparticle production. Furthermore, we investigate the influence of presynthesis pH on CNS characteristics, uncovering unexpected insights. The optimized CNS are subsequently evaluated for their sensing capabilities, demonstrating their ability to detect Cu^{2+} ions via both UV and fluorescence responses. Additionally, we explore the interaction of the CNS with various amino acids, revealing their sensitivity to Trp through a distinctive UV response alteration. To determine their environmental suitability, we analyze real water samples from diverse sources such as lakes, taps, and distilled water. This work introduces a facile and selective approach for Cu^{2+} and Trp sensing, with potential applications in various fields.

2. EXPERIMENTAL DETAILS

2.1. Materials and Instruments. The major raw material banana peels were obtained from the local market of Chandigarh in the name of "happy bananas". The commercially available chemicals such as metal salts, quinine sulfate, amino acids, etc. were procured from Sigma Aldrich. All of the chemicals used in experiments were not purified any further. For the characterization of nanospheres, UV−vis absorption and fluorescence emission spectroscopy analyses were performed, which determined the photophysical properties of nanospheres. The UV−Vis spectrum was recorded using a U-2900 spectrophotometer and for the fluorescence emission spectrum, a PTIQM40 spectrofluorometer (quartz cuvette and optical path length of 10×4 mm^2) was used. Deionized water was used as the solvent, and it was obtained from a Direct-Q3 UV water purification system. The imaging of nanospheres was done using TEM (transmission electron microscopy), and 3D modeling for size is done using AFM (atomic force microscopy). For elemental and compositional analysis, we performed X-ray photoemission spectroscopy using a Thermo Scientific K-Alpha with a monochromated, microfocused, low-power A1 K-α X-ray source. For analyzing the functional groups present on the nanospheres, FTIR (Fourier transform infrared) analysis was done, and for the IR spectra, we used a PerkinElmer FTIR spectrophotometer. The lifetime decay analysis of CNS in the presence and absence of Cu^{2+} was performed using time-correlated single photon counting (TCSPC) instrument of HORIBA DeltaFlex (using NL-C2 Pulsed Diode Laser). A digital pH meter was used to determine the pH value of the sample. For the synthesis of CNSs, an Anton Paar Monowave 300 Microwave Synthesis reactor with a MAS 24 autosampler was used to optimize the temperature, pressure, hold time, and pH. For real water sample testing, the samples were obtained from different water sources i.e., the lake sample was collected from Sukhna Lake, Chandigarh, India; the tap water sample was collected from Sector 39, Chandigarh, India; and distilled water was obtained from CSIR-IMTECH, Chandigarh, India.

2.2. Synthesis of Carbon Nanospheres (CNS). The method of producing CNS from banana peels includes grinding the banana peels in MQ water, setting the pH to the acidic range (3−4 pH) using acetic acid, placing the mixture in a microwave synthesizer at a pressure of 15 bar, increasing the temperature to 180 °C, holding the temperature for 15 min, cooling the sample to 55 °C, dispersing particles in MQ water, and purification of the sample. Briefly, 1 g of banana peels was ground using 1 mL of MQ water and the pH was set to 3 using a few droplets of acetic acid. It was further transferred to a G10 glass vial and kept in a microwave synthesizer reactor with a magnetic bead in it. The temperature was set to 180 °C for a hold time of 15 min and 600 rpm. The pressure of the synthesizer went to 15 bar.

2.2.1. Presynthesis Impact of pH on the Synthesis of CNS. The pH effect is studied in the presynthesis of CNS. The method for this includes grinding the banana peels in MQ water (1 g/mL) and setting the pH in 3 ranges i.e., acidic using acetic acid (3−4 pH), neutral with MQ water (7 pH), and basic using NaOH (11−12 pH). This was followed by keeping the ground mixture in a microwave synthesizer at 600 rpm each, with the temperature set to 180 °C, hold time of 15 min, and cooling temperature to 55 °C. The pressure in all increased to almost 15 bar. The sample was dispersed in Milli-Q (MQ) water and subjected to filtration and purification processes. Initially, the sample was filtered twice using Whatman filter paper (90 mm circles) and then passed through a syringe filter (pore size: 0.2 μm, diameter: 13 mm)

https://doi.org/10.1021/acsomega.3c07544
ACS Omega 2024, 9, 4555−4571

Table 1. Comparative Analysis of Reported Nanoparticles Synthesized Using Banana as a Precursor

sr. no.	particle synthesized	precursor used	particle size (nm)	method of synthesis	synthesis time	temp. (°C)	application	ref.
1	carbon dots	banana peels	3−6	hydrothermal	24 h	200	make activated carbon electrode	33
2	carbon nanodots	banana peels	1−10	oven and microwaves	2 h 40 min	200	Fe(III) sensing	34
3	N doped carbon dots	dwarf banana peels	4	hydrothermal and carbonization	24 h	200	fluorescent inks	35
4	NS doped carbon quantum dots	banana juice	1.27	hydrothermal	4 h	200	Cu(II) ion sensing	36
5	carbon nanostucture	banana peels	not specified	hydrothermal	variable	220	water splitting	37
6	carbon nanospheres	banana peels	35	microwave assisted	15 min	180	detect Cu^{2+} ions and tryptophan amino acid	current work

three times. Subsequently, the solution underwent centrifugation at 10,000 rpm for 10 min. The supernatant was separated, and the CNS solution was subjected to sonication in the dark for 30 min.

2.3. Preparation of Metal Ion Samples and Dilution in an Aqueous Medium of Cu^{2+} Ions. A stock solution of different metal ions was prepared. In this, the chloride salt of various metal ions such as LiCl, NaCl, KCl, $CaCl_2$, $ZnCl_2$, $MgCl_2$, $CoCl_2$, $PbCl_2$, $CuCl_2$, $MnCl_2$, $HgCl_2$, $NiCl_2$, $LaCl_3$, and NH_4Cl was dissolved in MQ water. For multimetal studies, 2.18 μL of the stock is added to 1998 uL of CNS solution (9.7 μg/mL), making the metal ion concentration to be 97 μg/mL. For concentration-based studies of Cu^{2+} in UV−visible and fluorescence spectra, 4 mg/mL of $CuCl_2$ was prepared in MQ water to do fluorescence titration studies in the stretch of 0.2 μg/mL to 40 μg/mL. Similarly, UV−visible titration studies were performed in the range of 0−10 μg/mL.

2.4. Preparation of Amino Acid Samples. A stock solutions of different amino acids, which include L-arginine, L-proline, L-aspartate, L-methionine, L-cysteine, L-glutamate, L-threonine, L-glycine, L-histidine, L-lysine, L-isoleucine, L-phenylalanine, L-serine, L-tryptophan, L-leucine, and L-valine, was prepared at a concentration of 88.8 mg/mL by dissolving in 5% HCl solution so as to make all the amino acids dissolve for multiple amino acid studies. For concentration-based studies, the Trp solution was prepared at 4 mg/mL in 5% HCl solution using MQ water. For titration studies, the Trp concentration was varied from 0 to 14 μg/mL with a CNS concentration of 12 μg/mL.

2.5. Sample Preparation for Various Characterizations. For UV−vis spectroscopy and fluorescence spectrophotometry, the purified CNS solution was dispersed in MQ water as per the required concentration. For sample preparation for AFM, the CNS solution of 100 μg/mL was prepared, and a fresh mica layer was cleaved to hold the sample on it. A drop of CNS solution was suspended on a cleaved mica surface and kept in the oven for drying at 40 °C. After a few minutes of drying, the leftover droplet was removed by an airflow. The concentration of CNS used for the FTIR analysis was 100 μg/mL. This solution was further checked for its functional groups using FTIR spectroscopy. For XPS analysis, a drop of CNS solution of 100 μg/mL was cast on a glass slide, followed by drying. For TEM imaging, drops of 100 μg/mL of synthesized CNS were dispersed on a copper mesh grid (carbon film on copper mesh grids by Tedpella USA). The grid was then kept under a transmission electron microscope to determine the size and shape of carbon nanoparticles.

2.6. Quantum Yield Calculations. The quantum yield of the prepared CNS was obtained using the formula in eq 1.[27] This requires the use of references. Here, for the measurement of quantum yield, quinine sulfate was used as a reference (quantum yield = 0.546 in 0.1 M H_2SO_4).[28,29] The working concentration of CNS was set to 10 mg/mL and the sample as well as the reference was excited at 350 nm in a fluorescence spectrophotometer.

$$\phi_S = \phi_R \times \frac{A_S . F_R . \eta_S^2}{A_R . F_S . \eta_R^2} \quad (1)$$

In this equation, S and R in subscript refer to sample and reference, respectively. ϕ_S stands for the emission quantum yield of the CNS sample and ϕ_R stands for the emission quantum yield of the used reference, F refers to the areas corresponding to emission bands, A refers to the absorbance of the CNS when they are excited, and η_S and η_R refer to the refractive index of solvent used in sample and reference, respectively.

2.7. Measurement of the Detection Limit (LD) and Quantification Limit (LQ). To calculate the detection limit and quantification limit eqs 2 and 3 were used, respectively.[27,30] The titration study of CNS with Cu^{2+} was performed when the sample was excited at 350 nm and the titration study with Trp was carried out in the UV range of 250−550 nm.

$$LD = \frac{3\sigma}{S} \quad (2)$$

$$LQ = \frac{10\sigma}{S} \quad (3)$$

Here, σ refers to the standard error of the CNS sample, which was calculated using a linear fit plot of concentration with signal (Figures S6 and S7) on excitation at 350 nm. S indicates the slope of the calibration curve. S was obtained by plotting the values between (I_0/I) and metal ion concentration $[Cu^{2+}]$ for calculating LD and LQ values for Cu^{2+}. "S" is determined by a plot between (A/A_0) and Trp concentration [Trp] for calculating LD and LQ for Trp. The concentration of CNS was maintained at 12 μg/mL for the titration experiment. The titration experiment was repeated thrice in both UV and fluorescence spectrophotometers.

2.8. Study on the pH Effect and High Salt Effect on Prepared CNS. The synthesized CNS were exposed to different pH conditions ranging from 1.0 to 14.0. The pH was shifted toward the acidic side using acetic acid and hydrochloric acid, whereas toward the basic side using sodium hydroxide. The final pH was determined by using a pH meter and checked for fluorescence spectra on excitation at 350 nm. To study the effect of high salt concentration, the synthesized

https://doi.org/10.1021/acsomega.3c07544
ACS Omega 2024, 9, 4555−4571

Scheme 1. Systematic Illustration of the Synthesis of CNS from Banana Peels Using Microwave Synthesizer

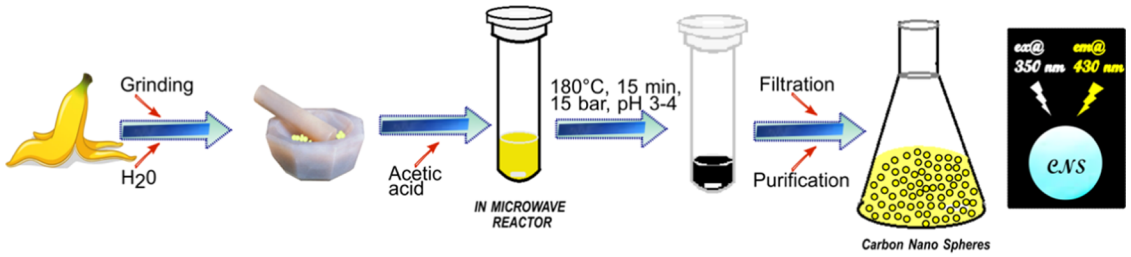

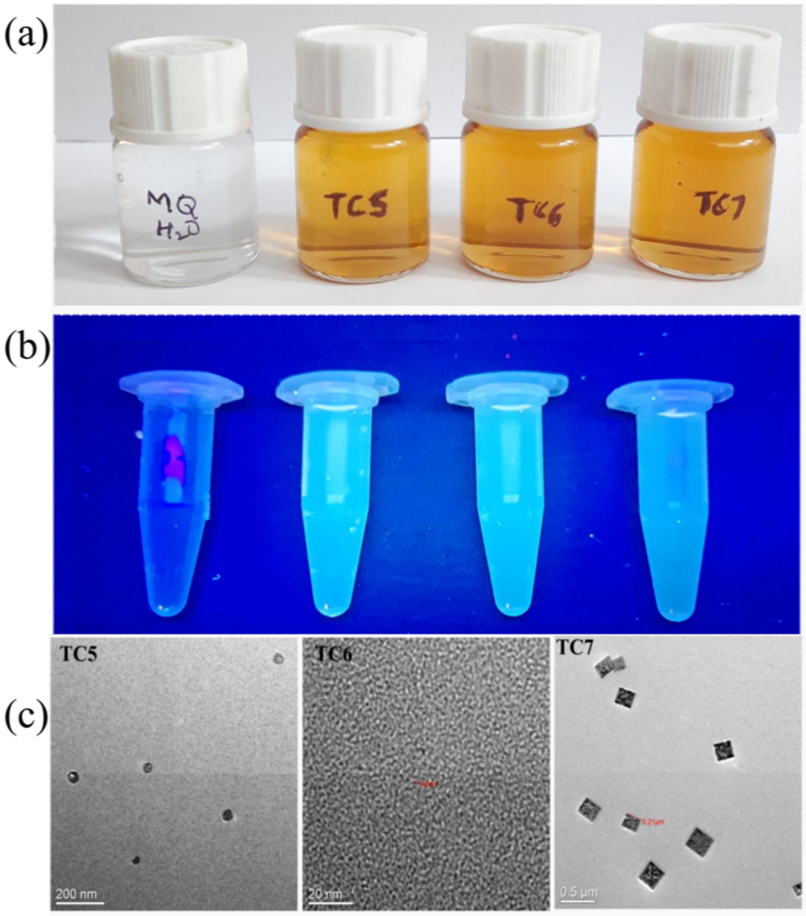

Figure 1. Presynthesis impact of pH where TC5 is in an acidic environment, TC6 in a neutral environment, and TC7 in a basic environment. (a) Image of TC5, TC6, and TC7 in visible light. (b) Image of TC5, TC6, and TC7 in UV light. (c) TEM image of TC5, TC6, and TC7 on specified scales.

CNS were exposed to high concentrations of NaCl and KCl dissolved in the aqueous medium.

3. RESULTS AND DISCUSSION

3.1. Detailed Synthesis and Study of the pH Effect on Presynthesis. To synthesize CNS, we used banana peels due to their richness in celluloses, hemicelluloses, and amino acids. As per the prior literature shown in Table 1, the hydrothermal reaction leads to a high synthesis time, so we chose to proceed with a microwave synthesizer to obtain a reduction in synthesis time and good quantum yield.

3.1.1. Detailed Synthesis Procedure of CNS. The synthesis of carbon nanoparticles demands a carbon-rich precursor, often fulfilled by carbohydrate-based sources in the bottom-up approach. Functionalization through appendages involves the utilization of amino acids, chemicals, or doping agents. In our pursuit of an efficient, eco-friendly synthesis route with improved functionalization, we turned to banana peels naturally occurring substance rich in celluloses, hemicelluloses, and amino acids.[31] A comparative analysis of nanoparticles synthesized using banana as a precursor molecule is presented in Table 1. In the realm of nanoparticle synthesis, microwave-assisted and hydrothermal methods each come with their own set of limitations, with the former yielding a low quantum yield and the latter entailing prolonged synthesis times.[30] Evidently, the conventional hydrothermal method suffers from lengthy synthesis times, low functionalization, and elevated costs, rendering it less economically feasible for various applications. Our endeavors succeeded in overcoming these limitations by devising a pioneering approach i.e., we used a microwave reactor-based synthesis. Employing a microwave reactor

https://doi.org/10.1021/acsomega.3c07544
ACS Omega 2024, 9, 4555−4571

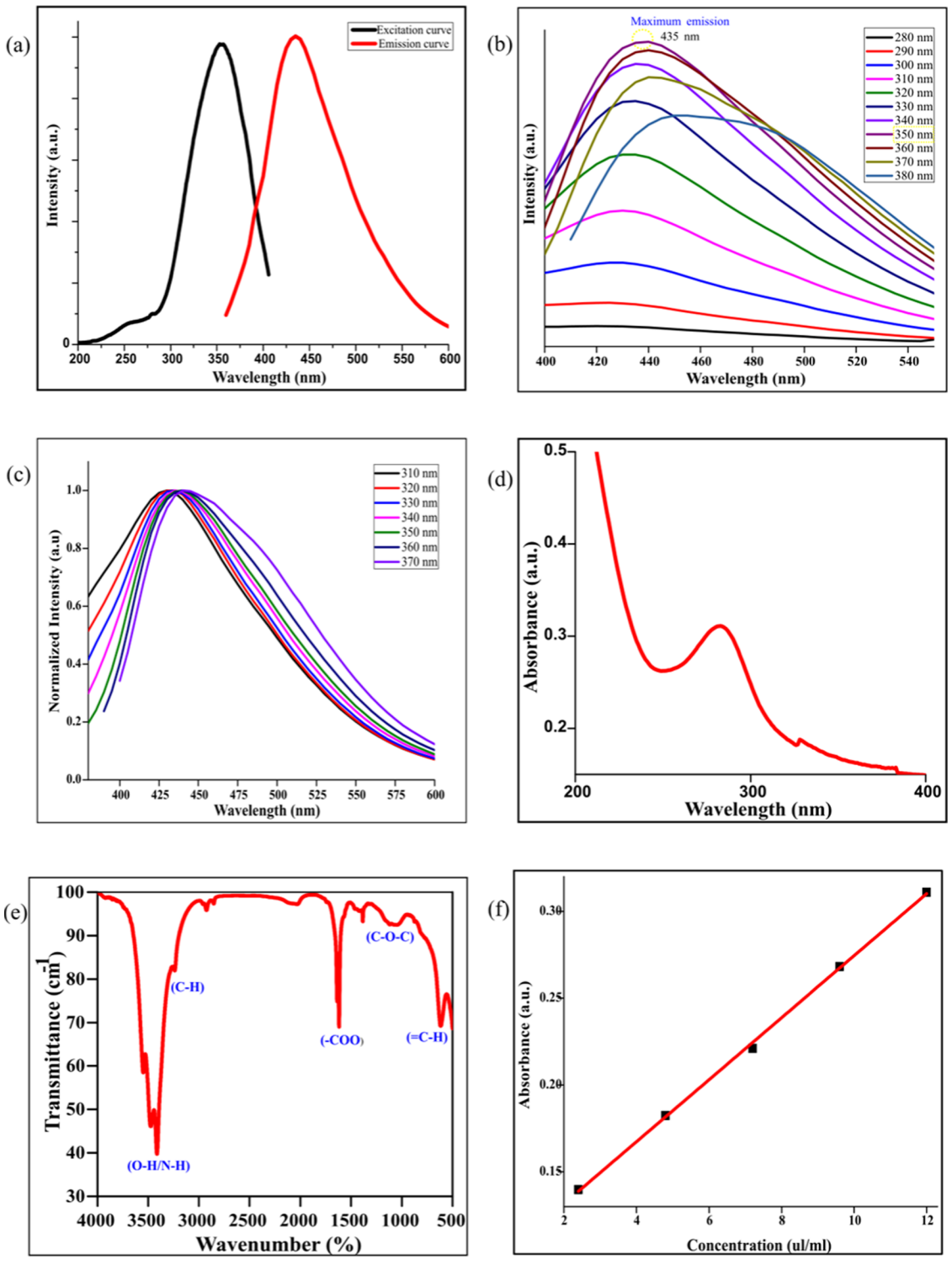

Figure 2. (a) Fluorescence excitation and emission spectrum of CNSs, (b) excitation-dependent fluorescence emission spectrum of CNS, (c) excitation-dependent fluorescence emission-normalized spectrum of the synthesized CNSs, (d) UV−vis spectra of synthesized CNSs at concentration of 12 μg/mL, (e) FTIR spectra of synthesized CNSs, and (f) concentration vs absorbance curve of CNSs for epsilon determination.

system enabled us to control temperature, pressure, and hold time conditions.[32] To synthesize nanoparticles, crushed banana peels dispersed in MQ water were introduced into the synthesizer, and conditions were optimized and fine-tuned to yield the desired product. Optimal conditions encompassed a temperature of 180 °C, a pressure of 15 bar, a hold time of 15 min, and a cooling temperature of 55 °C. The reaction was conducted at 600 rpm (Figure S4). Postreaction, the obtained product underwent filtration and purification. The schematic representation of the CNS synthesis process is depicted in Scheme 1.

Characterization of the synthesized carbon nanospheres involved several analytical techniques, confirming their successful synthesis and functionalization. UV spectroscopy,

https://doi.org/10.1021/acsomega.3c07544
ACS Omega 2024, 9, 4555−4571

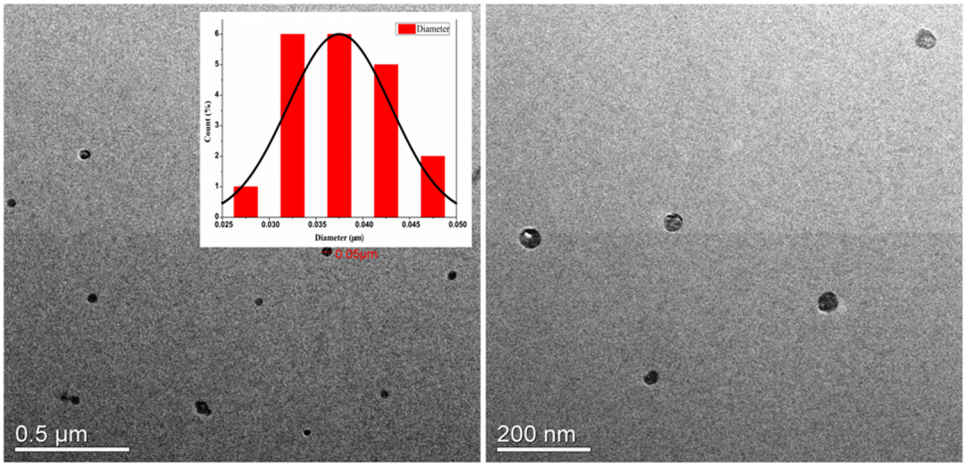

Figure 3. TEM (transmission electron microscopy) imaging of CNS (100 μg/mL) determining their size on the scale of 0.5 μm and 200 nm.

fluorescence spectrophotometry, XPS spectroscopy, TEM imaging, AFM analysis, and FTIR spectroscopy were employed to elucidate their properties. These analytical tools collectively facilitated a comprehensive understanding of the synthesized CNS, validating their potential for diverse applications. However, our innovative approach harnesses the advantageous properties of banana peels, minimizing the synthesis time, optimizing functionalization, and enhancing economic feasibility. This optimized methodology aligns with the principles of green chemistry, yielding a CNS primed for various sustainable applications.

3.1.2. Effect of pH on the Presynthesis of CNS. Exploring the influence of pH on nanoparticle assembly and synthesis is a novel avenue within the nanomaterial domain. Previous investigations rarely explored this aspect, thus motivating our inquiry into the pH effect on nanoparticle production. The present study sought to understand the correlation between pH conditions and the synthesis of nanoparticles, a dimension kept unexplored. For this purpose, we subjected ground banana peels to distinct pH conditions for important insights into the impact of presynthesis pH on the resulting nanoparticles. Our experimental design of this work has three key conditions: TC5, ground banana peels kept in an acidic pH range of 3−4 via acetic acid before putting them in a microwave reactor; TC6, maintained at neutral pH using MQ water; and TC7, maintained at a basic pH of 10−11 employing sodium hydroxide. The diversity of outcomes observed across the three samples has shown the significance of presynthesis pH modulation in nanoparticle formation.

Remarkably, TC5, characterized by its acidic pH, emerged as the most promising candidate, showcasing several desirable attributes. These nanoparticles demonstrated superior functionalization, intense fluorescence emission, monodispersity, spherical morphology, and increased water solubility. The presence of an acetyl group on the surface or within the core of the CNS likely contributes to this exceptional behavior. Consequently, due to their distinctive spherical configuration, these particles were referred to as CNS. In contrast, nanoparticles synthesized under neutral pH conditions (TC6) exhibited suboptimal attributes, characterized by a lack of monodispersity and a range of variable sizes, diminishing their suitability for further exploration. Similarly, particles generated under basic pH conditions (TC7) exhibited cubical or cuboidal morphologies, with sizes reaching up to approximately 200 nm making them unfit to fall in the nanomaterial range (Figure 1c). Visual representations of TC5, TC6, and TC7 under visible light and UV light, along with their TEM images, are illustrated in Figure 1, providing a comparative visual overview. Further substantiating these findings, Figure S1 presents a comprehensive comparative analysis of TC5, TC6, and TC7, encompassing their fluorescence, UV−vis, and FTIR spectra. Notably, TC5, characterized by its acidic pH, has emerged as the most competent, manifesting optimal characteristics like size, shape, functionalization, fluorescence intensity, and absorbance efficiency. Hence, there is a major role of pH in modulating the outcome of nanoparticle synthesis. The acidic pH environment not only facilitates the formation of monodisperse and highly functionalized CNS but also enhances their unique optical properties. This approach holds significance for expanding the horizons of nanoparticle design and engineering. Further studies deal with the applicability of TC5, determining its potential across several practical applications and industrial contexts.

3.2. Absorbance and Photoluminescence Properties of Carbon Nanospheres. To explore the influence of hydrophilic functional groups such as −OH and −COOH on nanoparticle surface stabilization, a comprehensive series of investigations was conducted, offering insights into the distinct properties of synthesized carbon nanospheres (CNSs). UV−vis spectroscopy and fluorescence spectroscopy were employed to decipher the absorbance and fluorescence behaviors, respectively. Fluorescence spectrum analysis revealed an optimal excitation wavelength for CNS at 350 nm, with an intense fluorescence emission peak at 430 nm (Figure 2a). Additionally, photoluminescence sensitivity to lamp excitation wavelengths between 280 and 380 nm was observed (Figure 2b), demonstrating the interplay between excitation and fluorescence emission (Figure 2c). Additionally, blue luminescence at a long UV wavelength of 365 nm further displayed the photoluminescence properties of the CNS (Figure 2b). UV−visible spectroscopy described the absorbance properties of CNS. The optical absorption spectrum exhibited a distinct peak at 282 nm in the UV range, attributed to the n−π^* transition of the C═O bond. A subsequent tail or low absorption spectrum at longer wavelengths corresponded to the π−π^* transition associated with conjugated C═C bonds (Figure 2d).

https://doi.org/10.1021/acsomega.3c07544
ACS Omega 2024, 9, 4555−4571

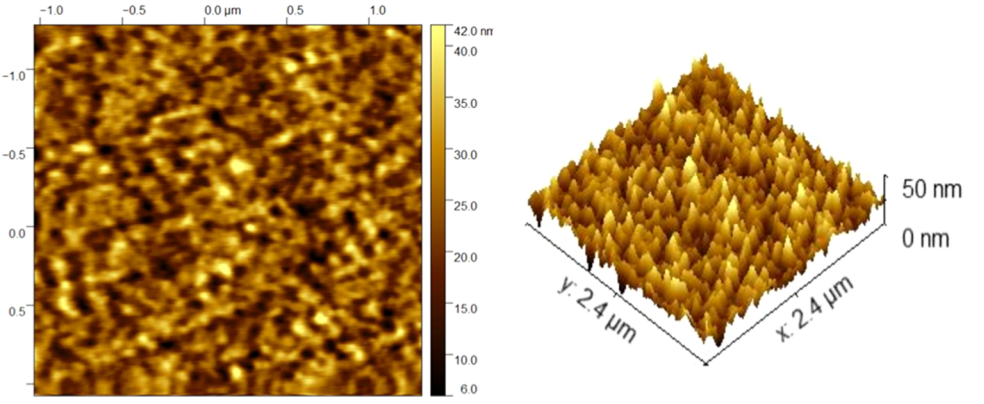

Figure 4. AFM (atomic force microscopy) of the synthesized CNSs at a concentration of 100 μg/mL.

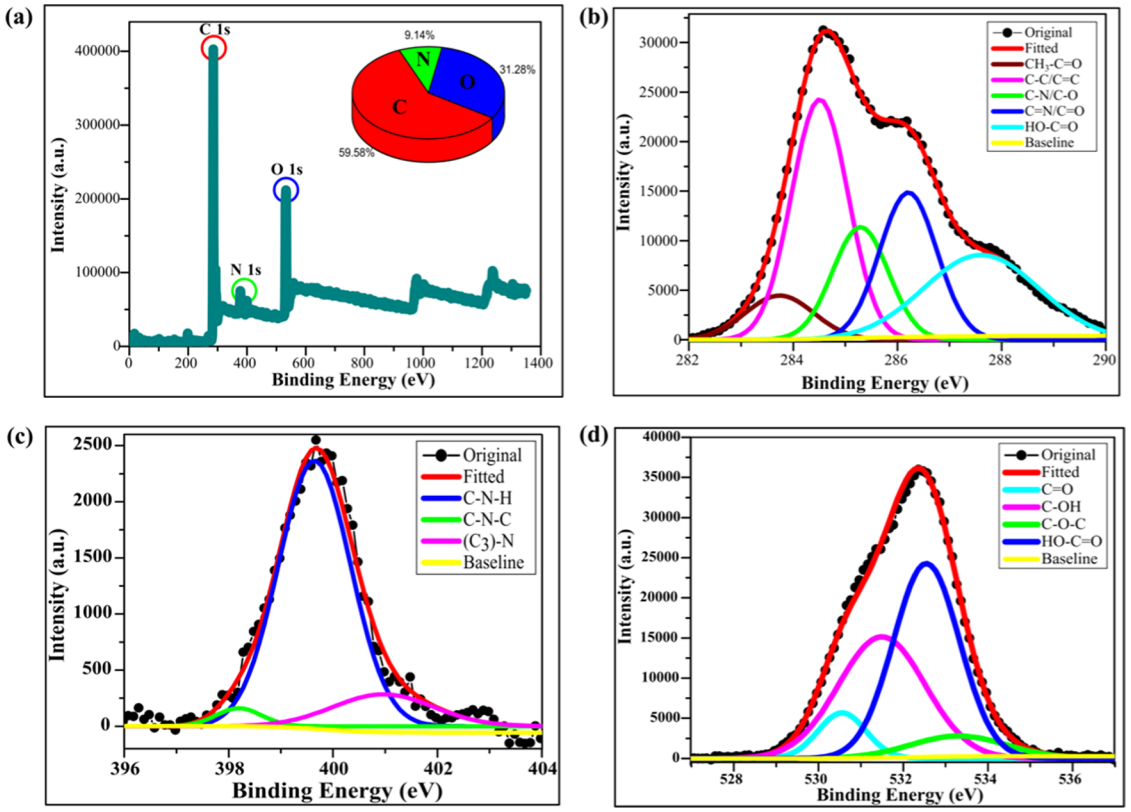

Figure 5. (a) Complete XPS survey spectra of CNS; deconvoluted spectra of (b) C 1s scan, (c) N 1s scan, and (d) O 1s scan.

These observations collectively reinforce the successful synthesis of CNSs and offer valuable insights into their optical properties. The optimal excitation wavelength and intense fluorescence emission peak suggest the potential of CNSs for applications in optical sensing and imaging. The excitation-dependent fluorescence behavior hints at the surface-sensitive nature of the photoluminescence process, possibly tied to specific functional groups. Furthermore, the diverse photoluminescence behaviors, including blue luminescence, open fields for the exploration of CNSs in multicolor imaging and labeling applications. The presence of distinct absorption peaks attributed to specific electronic transitions reflects the successful incorporation of hydrophilic functional groups on the CNS surface, underpinning their solubility and potential stabilization. These findings collectively represent the suitability of the CNS for various applications specific to their unique optical properties.

3.3. Structural Study of the Prepared Carbon Nanospheres. A comprehensive understanding of the structural properties of CNSs is essential for assessing their applicability and performance in various applications. To this end, an analysis of the CNS structure was conducted employing both high-resolution transmission electron microscopy (HR TEM) imaging and atomic force microscopy (AFM) analysis. The combination of these techniques offers complementary insights into the morphology and topography of the synthesized CNSs. The HR TEM imaging (Figure 3) provides a profound visualization of the structural characteristics of CNSs. The images reveal a consistent and uniform morphology, with the nanoparticles adopting a distinct spherical shape. Notably, the diameters of these CNSs range between 30 and 40 nm,

https://doi.org/10.1021/acsomega.3c07544
ACS Omega 2024, 9, 4555−4571

capturing the variance inherent to the synthesis process. Further statistical analysis of these dimensions yielded a mean size of 35 nm, consolidating the homogeneity of the nanoparticle population. Complementing the HR TEM observations, AFM analysis (Figure 4) offers an additional dimension to the structural study of CNS. The 3D AFM image elucidates the size distribution seen in TEM analysis, depicting a similar size range of 30−35 nm. This concurrence between HR TEM and AFM reinforces the accuracy of the size assessment and the consistency of the nanoparticle synthesis process. In a broader context, the homogeneity of CNS size and morphology has implications for their behavior in applications such as sensing, drug delivery, and catalysis. A consistent size distribution is essential for ensuring consistent and predictable interactions with target molecules or substrates. Hence, the structural study of CNSs through HR TEM imaging and AFM analysis showcases the successful synthesis of spherical carbon nanospheres with a mean diameter of 35 nm.

The compositional and structural analysis using XPS characterization was performed using high-resolution XPS spectra. The survey spectrum depicted the presence of peaks at 532.08, 285.08, and 399.08, which correspond to O 1s, N 1s, and C 1s, respectively (Figure 5).[38,39] The deconvolution of C 1s spectra is shown in Figure 5b, which suggests the presence of 5 peaks at 283.72, 284.52, 285.30,286.20, and 287.65, which corresponds to $CH_3C{=}O$, C−C/C═C, C−N/C−O, C═N/C═O, and HO−C═O, respectively.[69,70] Figure 5c shows the deconvolution of N 1s spectra, which indicates the presence of 3 different peaks at 398.14, 399.68, and 401.05, which signifies the presence of C−N−C, C−N−H, and (C_3)−N bond, respectively.[40−42] The high-resolution spectra of the O 1s scan can be seen in Figure 5d and after deconvolution, it has 4 peaks at 530.56, 531.52, 532.56, and 533.42, which represent the functional groups as C═O, C−OH, C−O−C, and HO−C═O, respectively.[43−45] We also determined the elemental analysis of C, N, and O, which comes out to be 59.58, 9.14, and 31.28%, respectively. The presence of these highly electronegative groups on CNS may be attributed to the binding of a highly positive divalent ion of Cu^{2+} making it a potential sensor.

3.4. Surface Charge and Functional Group Studies of CNS. The exploration of surface charge and functional groups on synthesized CNS is essential for understanding their chemical properties and potential applications. In this regard, Fourier transform infrared (FTIR) spectroscopy was employed as a powerful analytical tool. By the principle that distinct functional groups induce characteristic vibrational modes, FTIR spectroscopy enables the identification of various covalent bonds within the CNS. FTIR analysis of the CNS revealed a spectrum rich in informative features, with each corresponding to specific functional groups. Notably, an intense peak was observed at 3409 cm^{-1}, indicative of the presence of −OH/−NH groups on the CNS surface. The appearance of this peak exhibits the hydrophilic nature of the synthesized CNS, aligning with its water solubility and potential interaction with aqueous environments. Additionally, a sharp peak at 3235 cm^{-1} was observed, corresponding to the characteristic C−H bond. The abundance of this hydrocarbon bond in banana peels, a primary precursor for CNS synthesis, is attributed to the celluloses and hemicelluloses naturally occurring within the peels. This observation highlights the inherent contribution of the precursor material to the functionalization of CNS. Further analysis of the FTIR spectra revealed a sharp and narrow peak at 1629 cm^{-1}, which refers to the −COO bond's presence. This acetyl group could have originated from acetic acid or amino acids inherent to banana peels. The presence of this bond enhances the functionalization of CNSs and their sensitivity to precursor constituents. The broad peak observed at 1083 cm^{-1} corresponds to the presence of the C−O−C bond, contributing to the complex array of functional groups present on the CNS surface. Similarly, a peak at 611 cm^{-1} is attributed to the ═C−H bond functionalization, offering diverse chemical species within the CNS framework.[46]

FTIR analysis unveils their chemical compositions and potential reactivity. The observed −OH/−NH groups ensure the potential for interactions with polar molecules and hence will be competent for applications such as molecular sensing or surface modification. The prevalence of the C−H bond ensures that the synthesis process preserves certain attributes of the precursor material. The identification of the −COO bond and the C−O−C bond further amplifies the functional diversity of CNSs. These functional groups not only offer potential points for surface modifications but also determine the potential of CNSs to engage in chemical interactions relevant to catalytic or adsorption processes. Hence, the FTIR-based exploration of CNS functional groups serves greatly in understanding their chemical properties and potential applications. The findings validate the successful functionalization process, paving the way for their utilization in practical applications.

3.5. After Effect of pH and High Salt Concentration on Photoluminescence Properties of the Prepared Carbon Nanospheres. The alteration of photoluminescence properties in response to pH variations is a crucial aspect of nanoparticle functionality and applicability. To explore the pH-dependent behavior of the prepared CNS, an investigation into their fluorescence spectral response was conducted. The photoluminescence behavior of the CNS was systematically investigated across a broad pH range, spanning from pH 1 to 14 as shown in Figure 6. This pH variation of one unit provided insights into the nanosphere's fluorescence response

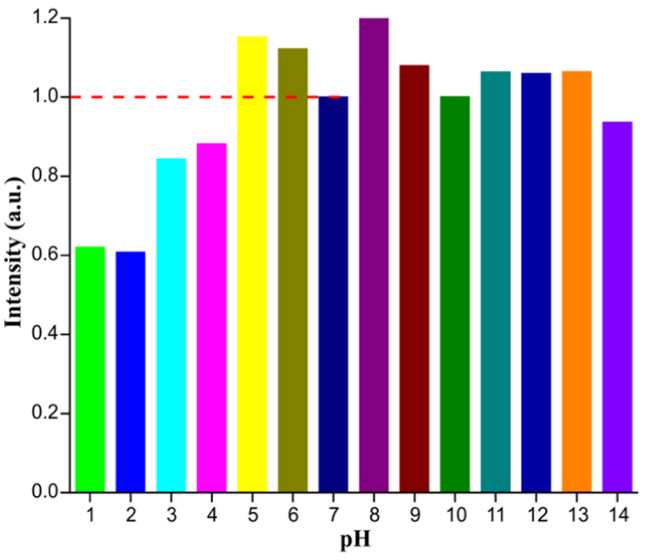

Figure 6. Effect of pH on fluorescence emission peak at 430 nm when excited at 350 nm for synthesized CNS (excitation @ 350 nm, emission @ 430 nm).

https://doi.org/10.1021/acsomega.3c07544
ACS Omega 2024, 9, 4555−4571

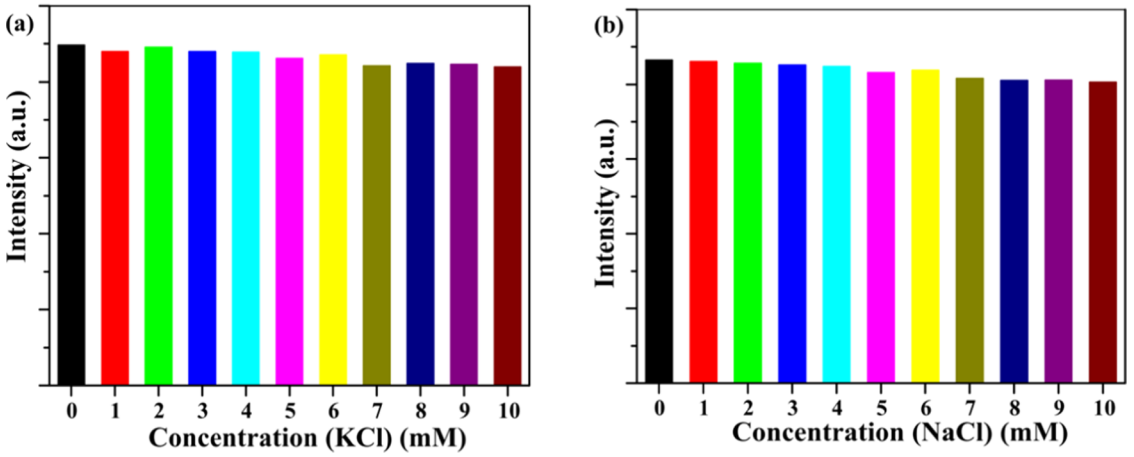

Figure 7. Effect of high salt concentration (a) KCl and (b) NaCl on the fluorescence emission peak at 430 nm when excited at 350 nm for synthesized CNS (excitation @ 350 nm, emission @ 430 nm).

Table 2. Comparison of Nanoparticles from Organic Precursors with the Synthesized CNSs

sr. no.	raw material	synthesis time	methodology	λ_{ex} (nm)	λ_{em} (nm)	QY (%)	application	ref.
1	pear	2 h	hydrothermal	360	450		sense Cu^{2+} ions	51
2	papaya	0.5−1 h	hydrothermal	330		23.7	detect Fe^{2+} ions	52
3	banana juice	4 h	hydrothermal	330	420	32	detect Cu^{2+} ions	12
4	spinach	6 h	solvothermal	440	680	15.34	bioimaging	50
5	banana peel	24 h	hydrothermal	345	413	23	detect Fe^{3+}, fluorescent ink	53
6	bamboo leaves	24 h	solvothermal	400	493	4.7	detect Pb^{2+} and Hg^{2+} ions	54
7	rice residue	12 h	hydrothermal	440	500	23.48	detect Fe^{3+} ions	55
8	peach	5 h	hydrothermal	310	400	15	ORR	56
9	mango peel	6 h	carbonization	310	420	8.5	cell labeling, detect Fe^{2+} ions	57
10	banana juice	24 h	hydrothermal	355	429	20	bioimaging	48
11	pipe tabacco	8 h	hydrothermal	369	450	3.2	detect Cu^{2+} ions	58
12	watermelon	3 h	hydrothermal	355	439	10.6	cell imaging, detect Fe^{3+} ions	59
13	sugar cane juice	6 h	hydrothermal	350	500	10.7	detect Cu^{2+} ions	60
14	pineapple	3 h	hydrothermal	370	453	10.06	detect Cr(VI)	61
15	sago waste	1 h	pyrolysis	350	390		detect Cu^{2+} and Pb^{2+} ions	49
16	grape	6 h	thermolysis	435	498	32.1	detect Cu^{2+} and S^{2-}	47
17	lemon juice	12 h	hydrothermal	420	525	21	detect V^{5+}	62
18	banana peel	15 min	microwave assisted	350	430	12.4	detect Cu^{2+} and Trp	current work

to differing acidity and alkalinity levels. The fluorescence emission spectra of CNSs exhibited great trends in response to varying pH levels. When subjected to pH changes toward the basic side, the intensity of fluorescence showed minimal variation. This observation hints at the inherent stability of the CNS photoluminescence properties in alkaline environments. Conversely, a notable decrease in photoluminescence intensity was noted when pH values dropped below 3 units. Under these strongly acidic conditions, the fluorescence intensity of the CNS was quenched by approximately half of its original intensity. This pH-dependent quenching phenomenon suggests potential interactions between the acidic environment and the luminescence properties of CNSs. Hence, the investigation led to a certain conclusion regarding the optimal pH range within which the CNS can effectively serve as a sensor. Specifically, the effective pH range spans from 4 to 14 units. Within this range, CNS exhibit stability in their photoluminescence properties, making them promising candidates for sensing applications. The minimal variation observed on the whole aligns with the inherent stability of the CNS photoluminescent characteristics, which is of significant importance. Additionally, the effect of the high salt concentration was explored by using standard salts, such as KCl and NaCl. Figure 7a shows the effect of increasing the concentration of KCl from 1 to 10 mM on the fluorescence of CNS when excited at 350 nm. Figure 7b shows the effect of increasing the concentration of NaCl from 1 to 10 mM. In both graphs, there is a minimum alteration in the fluorescence emission peak. Hence, the synthesized CNS are found to be stable in highly saline environments and have a wide working pH range which makes them a competent sensor for potential applications in physiological and biological contexts.

3.6. Quantum Yield of the Synthesized Carbon Nanospheres. The exploration of the quantum yield in the context of synthesized CNS determines their photophysical performance. In nanoparticle synthesis, organic precursors have received attention for their capacity to yield nanoparticles with several attributes, ranging from elevated quantum yields[47] to attributes such as diminished toxicity,[48] cost-effectiveness,[49] and compatibility within biological systems.[50] Notably, the inherent interlinking properties embedded in banana peels hold promise for producing functional carbon nanoparticles. Employing the method elucidated earlier, the transformation of banana peels into carbon quantum spheres yielded a quantum

https://doi.org/10.1021/acsomega.3c07544
ACS Omega 2024, 9, 4555−4571

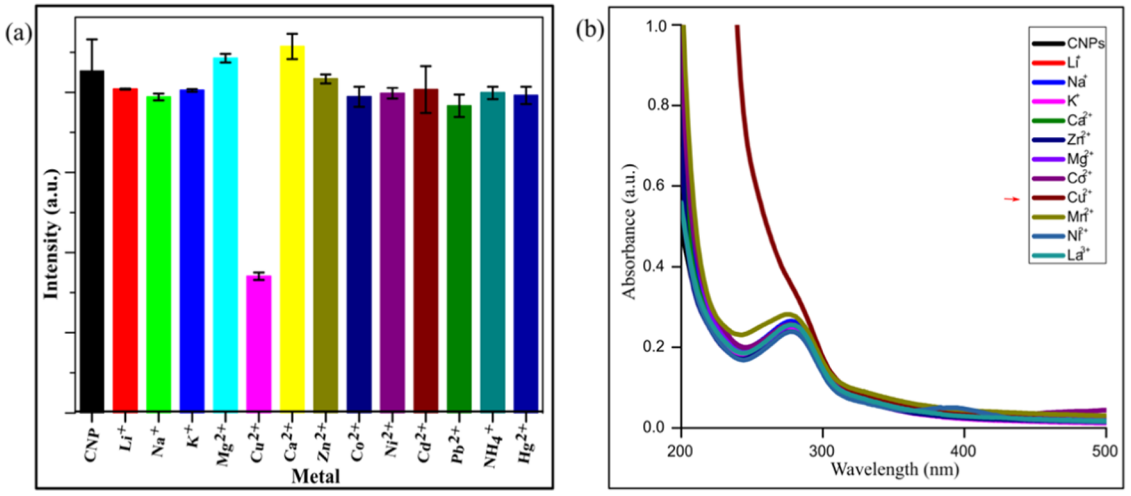

Figure 8. Comparative multimetal analysis of CNS using fluorescence and UV spectra. (a) Fluorescence intensity of CNS with various metal ions at 430 nm when excited at 350 nm. (b) UV−vis spectra of CNS with different metal ions in an aqueous medium.

yield of 12.4%. The achieved quantum yield of 12.4% assumes particular significance in the realm of nanoparticle luminescence. Although not reaching the perfect efficiency, this quantum yield conveys that a notable fraction of absorbed photons successfully transitions into emitted photons. Considerations for further optimization could involve investigating parameters such as precursor concentration, reaction conditions, and surface passivation to enhance the quantum yield and, consequently, the luminescence performance. In Table 2, a comparative analysis of nanoparticles synthesized from diverse natural precursors is presented. Within this comparative framework, the quantum yield of 12.4% showcased by the CNS emerges as an appreciable value, aligning well with or even surpassing the luminescence efficiencies of other nanoparticles synthesized from natural sources. A firm dimension of this investigation lies in the pH-dependent synthesis approach. This approach not only contributes to enhancing the quantum yield of CNSs but also complies with green chemistry by reducing the synthesis duration. While the journey toward achieving maximal quantum efficiency continues, the observed quantum yield aligns with benchmarks already established by other naturally derived nanoparticles.

3.7. Detection of Cu^{2+} Ions in an Aqueous Medium. In order to understand the binding ability and modulation in the photophysical properties of the synthesized CNSs, the absorption and emission spectra of the CNS were observed in the presence of different metal ions.

3.7.1. Comparative Studies: Investigating Cu^{2+} Ion Detection. The capability of the synthesized CNS solution for Cu^{2+} detection was elucidated through comparative studies that contained fluorescence quenching analyses, along with multimetal UV spectra investigations. These investigations collectively demonstrate the potential of the CNS as a robust sensor for Cu^{2+} ions. Figure 8a presents a visual representation of the fluorescence quenching phenomenon exhibited by CNSs in response to multiple metal ions. Cu^{2+} ions demonstrated a remarkable capability to efficiently quench the fluorescence emitted by the CNS, quenching it to more than half of its original fluorescence intensity. This profound quenching behavior infers the dynamic interplay between the CNS and Cu^{2+} ions. This further considers the synthesized nanoparticles optimal for Cu^{2+} detection. Further, upon investigation of the multimetal UV spectra analysis, as depicted in Figure 8b, we found Cu^{2+} to significantly cause UV spectra changes. The emergent red-shift in the UV spectra stands as evidence of the show CNS−Cu^{2+} interaction. This red-shift phenomenon is related to the possibility of a distinct accumulation or complexation event due to the intermolecular interplay between CNS and Cu^{2+} ions.

The dual demonstration of fluorescence attenuation and UV spectral alterations underlines the dominance of static quenching in the CNS−Cu^{2+} interaction. This static quenching manifests as the formation of nonfluorescent complexes arising from the binding of CNS and Cu^{2+} ions through molecular interactions like chelation or coordination. In the broader context, the observed quenching and spectral changes comply well with well-established fluorescence quenching theories. The quenching process, caused by energy transfer from the excited state of the CNS to Cu^{2+} ions, stands as a plausible mechanism contributing to fluorescence attenuation. Consequently, comparative studies present a solid foundation for the effectiveness of CNS as a Cu^{2+} ion detector. The coordination of fluorescence quenching dynamics, multimetal UV spectral alterations, and inferred static quenching mechanisms collectively proves the potential utility of the CNS−Cu^{2+} interaction. These insights could consider CNS as a potent tool for analyte detection in diverse applications.

3.7.2. Competitive Studies: Assessing Selectivity of CNS toward Cu^{2+}. An examination of the interaction dynamics between the CNS and Cu^{2+} ions compelled further investigation of the potential impact of diverse ions on fluorescence intensity. Competitive studies were conducted to explore the effect on the CNS in the presence of various ions, including Li^+, Na^+, K^+, Ca^{2+}, Mg^{2+}, Zn^{2+}, Co^{2+}, Pb^{2+}, Mn^{2+}, Ni^{2+}, La^{3+}, and NH_4^+. These studies sought to check the degree of Cu^{2+} ion quenching in the presence of competing ions, providing insights into the specificity and selectivity of CNSs as a potential sensor. Figure 9 displays the outcome of these competitive studies. Remarkably, it is seen that the presence of diverse ions exerts a negligible effect on the quenching phenomenon induced by Cu^{2+} ions, and this holds significant implications. It signifies the robust specificity and selectivity of CNSs as a sensor for Cu^{2+} ions. The absence of interference is

https://doi.org/10.1021/acsomega.3c07544
ACS Omega 2024, 9, 4555−4571

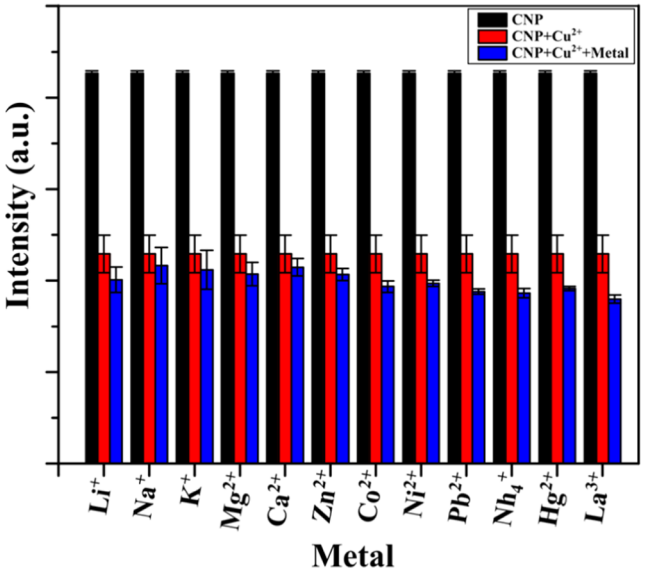

Figure 9. Competitive effect of diverse multivalent ions on the fluorescence intensity of the CNS (9.8 μg/mL) and the CNS−Cu^{2+} complex.

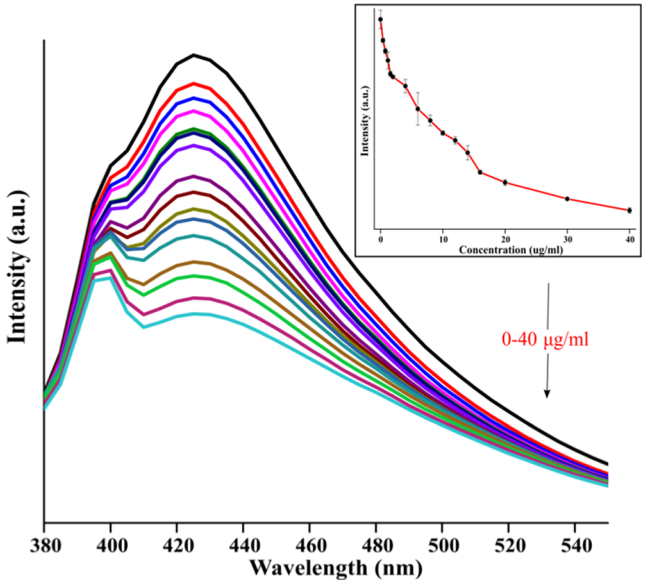

Figure 10. Effect on fluorescence spectra of CNSs (12 μg/mL) with increasing concentration of Cu^{2+} ions (0−40 μg/mL).

attributed to the distinctive binding interactions between CNS and Cu^{2+} ions, where complexation occurs irrespective of other multivalent ions. The preservation of quenching efficacy makes it a better choice for analyte detection in complex ion environments.

3.7.3. Titration Studies: Determining the Cu^{2+} Interaction Dynamics. To unravel the interaction dynamics between CNSs and Cu^{2+} ions, titration studies were performed. Fluorescence and UV−vis spectrum titration curves provided insights into CNSs' responsiveness to increasing Cu^{2+} ion concentrations. In the fluorescence spectrum titration curve (Figure 8), an evident decrease in fluorescence intensity was observed with increasing Cu^{2+} ion concentrations (0−40 μg/mL), showing the sensitivity of the binding event. The synthesized CNSs showed a linear response within a concentration range of 0−40 μg/mL (Figure 10). The UV−vis spectrum titration curve extended the investigation, revealing a red-shift in the presence of increasing Cu^{2+} concentrations (Figure 9), indicative of electronic transitions modulation.[63] Also, a linear increase in the UV−vis spectral peak at 282 nm was observed within the concentration range of 0−8 μg/mL (Figure S8), contributing to the spectrum of CNS's detection capabilities. These linear detection profiles align with the permissible and relevant concentration ranges of Cu^{2+} ions in environmental and biological samples, thereby emphasizing the practical applicability of the CNS as a selective and sensitive sensor.

3.7.4. Proposed Sensing Mechanism of Cu^{2+} with Carbon Nanospheres. The synthesized CNSs boast an intricate composition characterized by their inherent negative charge and a diverse array of surface functional groups. Notable functional groups include O−H, COOH, C═O, C−O−C, N−H, and ═C−H. This unique composition positions the synthesized CNS as a robust platform for the detection of Cu^{2+} ions, with these functional groups forming the basis of its sensing mechanism. The surface functional groups, specifically those appended with O−H, COOH, and others, create an environment conducive to interactions with Cu^{2+} ions. The alteration in the emission maximum upon interaction with Cu^{2+} can be attributed to various mechanisms, including photoinduced electron transfer (PET), intramolecular charge transfer (ICT), and photoinduced charge transfer (PCT). Notably, metal ions from the main groups, characterized by high charge density and electropositivity, can lead to either enhancement or quenching of fluorescence. Fluorescence titration experiments, as depicted in Figure 10, illustrate a uniform quenching of CNS fluorescence intensity with increasing Cu^{2+} concentration.[64] This consistent quenching is attributed to complexation, which hinders the electron-releasing capacity of CNS, resulting in a quenching behavior.[65−67] Hence, the mechanism behind the quenching in the presence of Cu^{2+} ions is CHEQ i.e., chelation-enhanced quenching as depicted in Scheme 2. The Irving−Williams rules further emphasize the strong complexation ability of Cu^{2+} ions compared with other divalent first-row transition-metal ions.

Additionally, the quenching type was investigated to discern whether it is static or dynamic. Stern−Volmer plots, presented in Figure S7, display a linear variation with increasing quencher concentration, indicative of static quenching.[68] Lifetime studies (Figure 11) were performed in the presence and absence of Cu^{2+} ions. The average fluorescence lifetime value in the absence and presence of Cu^{2+} comes out to be 1.82 and 1.73 ns, respectively. This reconfirms the static quenching nature, as all binding sites are filled upon the binding of Cu^{2+}, resulting in a fixed or invariable excited state lifetime or the formation of a new complex with Cu^{2+} ions.[69] Furthermore, the increasing concentration of Cu^{2+} in CNSs is observed to distort the absorption spectra, as shown in Figure S8, reinforcing the static quenching nature. This distortion suggests that the synthesized CNSs operate as a "turn-off" fluorescence sensor for Cu^{2+} ions due to the static quenching phenomenon.[70,71] In conclusion, the synthesized CNS, characterized by its negative surface charge and the interaction potential of its diverse functional groups, serves as an effective 'turn-off' fluorescence sensor for Cu^{2+} ions due to the CHEQ (chelation-enhanced quenching) effect. The elucidation of static quenching mechanisms through fluorescence titration, Stern−Volmer plots, and lifetime studies enhances our understanding of the intricate

https://doi.org/10.1021/acsomega.3c07544
ACS Omega 2024, 9, 4555−4571

Scheme 2. Systematic Illustration of the Sensing Mechanism of Cu^{2+} by the Synthesized CNSs

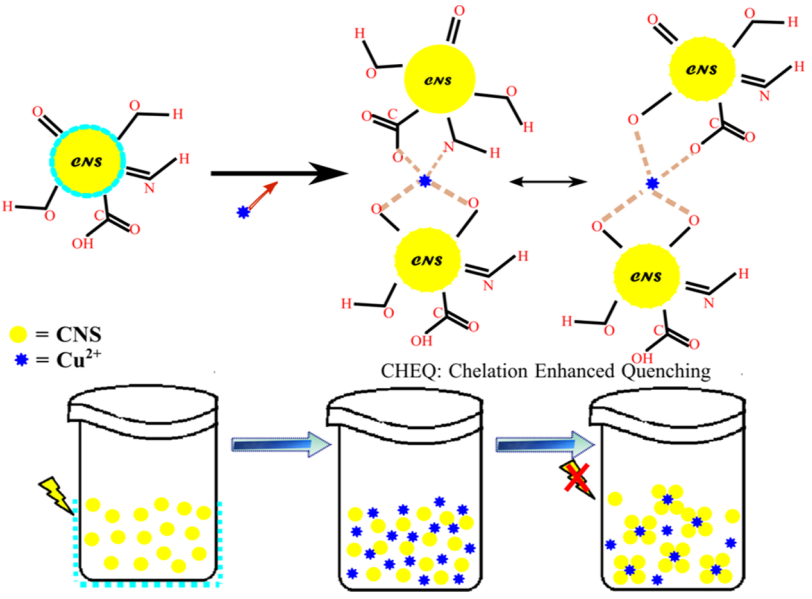

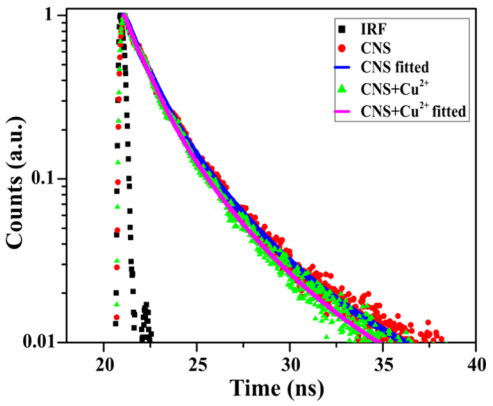

Figure 11. Fluorescence lifetime studies for CNS and CNS + Cu^{2+} ions with the fitting using a third exponential function.

sensing capabilities of the synthesized CNS in the presence of Cu^{2+} ions.

3.7.5. Determination of the Detection Limit and Quantification Limit for Cu^{2+}. The assessment of the sensitivity of the synthesized CNSs to detect Cu^{2+} ions can be understood by the determination of detection and quantification limits. These were determined through fluorescence titration studies involving the CNS (12 μg/mL) subjected to various Cu^{2+} titrations. The comprehensive methodology employed is elucidated above. The fluorescence titration studies involve understanding the change in fluorescence intensity of CNS (12 μg/mL) in the presence of varying Cu^{2+} concentrations, spanning from 0 to 40 μg/mL. These studies were conducted in triplicate, and the mean values were derived and plotted. The resultant plot (Figure 10) shows a graphical depiction of the intensity quenching phenomena observed as Cu^{2+} concentrations increase.

For the determination of detection and quantification limits, a linear plot showcasing the relationship between the Cu^{2+} concentration and fluorescence intensity was obtained. The fluorescence intensity peak at 430 nm was obtained in terms of I_0/I, the ratio of fluorescence intensity upon excitation at 350 nm. The standard deviation (σ) for the calculations was derived from multiple readings of the blank, while the slope (S) was obtained in Figure S7. By using the established formula $3\sigma/S$ for the detection limit and $10\sigma/S$ for the quantification limit,[64,72,73] the detection limit and quantification limits were precisely calculated. The determined values for the detection and quantification limits emerged as 0.736 and 2.45 μg/mL, respectively. These values show the capability of CNS in detecting even minute concentrations of Cu^{2+} ions. The obtained detection and quantification limits have great significance. The quantification limit of 2.45 μg/mL implies that the synthesized CNS is a powerful analytical tool, capable of reliably quantifying Cu^{2+} ions. However, the detection limit of 0.736 μg/mL shows the remarkable ability of CNS to detect Cu^{2+} ions at ultralow concentrations, surpassing the recommended limits for Cu^{2+} ions in both biological and environmental samples.[74] This reinforces the ability of synthesized CNS in real-world analytical scenarios, especially in contexts where trace Cu^{2+} detection is of paramount importance. Hence, the determination of detection and quantification limits provided the practical relevance of the CNS in trace detection scenarios.

3.8. Detection of Tryptophan Amino Acid (UV–Visible Response). The feasibility of the prepared CNSs for amino acid sensing was probed, revealing their interaction dynamics. Surprisingly, the CNS fluorescence remained unaltered in most interactions, suggesting the nonengagement of the specific functional groups responsible for fluorescence. However, a notable red-shift as well as peak amplification emerged in the CNS UV spectra upon interaction with the Trp amino acid, hinting at distinctive intermolecular dynamics.

3.8.1. Comparative Studies: Deciphering the L-tryptophan Amino Acid Interaction. The interaction of CNSs with diverse amino acids was explored through a comprehensive comparative study using UV spectral analysis (Figure 12). This study illuminated the multifaceted interaction dynamics between the CNS and various amino acids, unraveling response patterns. The UV spectra were obtained in the presence of different amino acids. Interestingly, several amino acids, including L-arginine, L-glutamate, L-proline, L-glycine, L-threonine, L-histidine, L-isoleucine, L-valine, L-leucine, L-

https://doi.org/10.1021/acsomega.3c07544
ACS Omega 2024, 9, 4555−4571

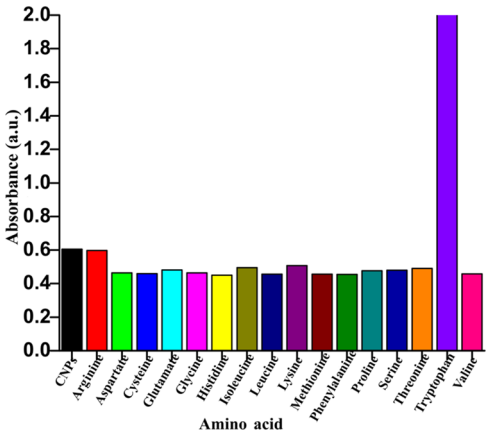

Figure 12. Effect of different amino acids on UV spectrum peak at 282 nm for the CNS (12 μg/mL).

aspartate, L-lysine, L-cysteine, L-phenylalanine, L-serine, and L-methionine, depicted minimal alteration in the UV spectra. The absorbance peak at 282 nm, the signature of CNS's presence, remained stable in the presence of these amino acids. However, the interaction with L-tryptophan depicted a distinctive response. The introduction of Trp ignited a complex procedure for spectral shifts. Notably, a red-shift, along with the amplification of the UV peak at 282 nm, emerged. This unique response, exclusive to Trp, sets it apart from its amino acid counterparts. In contrast to other amino acids tested, Trp's distinctive spectra hint at specific intermolecular forces at play, possibly involving electronic transitions catalyzed by its aromatic ring system. This comparative study forms the foundation for deeper explorations. Further investigations dealt with concentration-based studies to understand the in-depth mechanism of intramolecular and intermolecular changes induced by the interaction of Trp with the synthesized CNS.

3.8.2. Titration Studies: Investigation into L-tryptophan's Interaction Dynamics. The investigation into varying concentrations of L-tryptophan yielded interesting titration curves (Figure 13). These curves revealed a consistent trend of red-shift phenomena coupled with enhancements in absorbance at 282 nm − a wavelength corresponding to the peak observed in the UV spectra of the synthesized CNS. This corresponds to the interplay between Trp and CNS, demonstrating how alterations in the concentration modulate the observed spectral behavior. This outcome is observed in the linear detection range of 0−14 μg/mL. This range signifies the extreme sensitivity of the CNS-based detection system, making it suitable for quantifying amino acids within biological samples. The detection of such minute concentrations underscores the analytical potential of the synthesized CNS and makes it competent for biosensing industries.

3.8.3. Proposed Sensing Mechanism of L-tryptophan with the Synthesized CNS. The interaction between the CNS and Trp gives rise to a distinctive spectral response, characterized by a significant red-shift and an amplified absorbance peak at 282 nm. The exploration to understand the mechanism of interaction requires firm consideration of this unique interaction phenomenon and the spectral alterations. This spectral transformation can be attributed to a specific interplay between the CNS and Trp, which triggers a distinct change in electron transfer dynamics. This change, in turn, is responsible for the spectral red-shift and absorbance peak enhancement

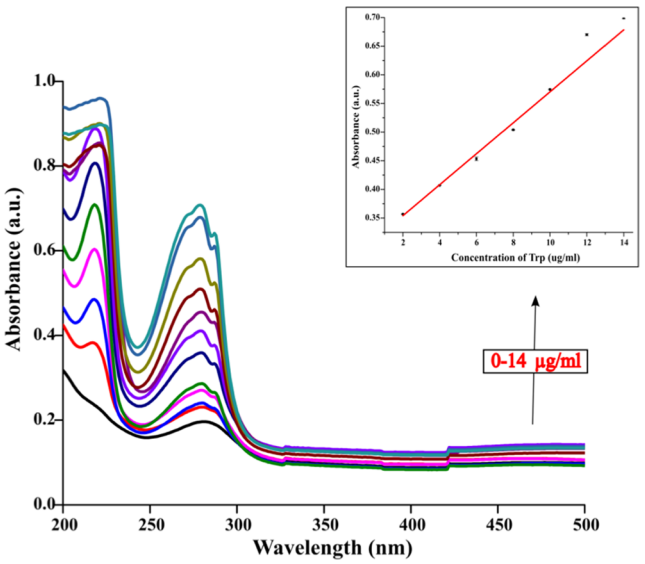

Figure 13. Effect on UV−visible spectra of CNS (12 μg/mL) with increasing concentrations of L-tryptophan amino acid (0−14 μg/mL).

observed in the UV spectra. Notably, the absence of any fluorescence alteration upon interaction with Trp implies that the fluorophore moieties of CNS remain uninvolved in this interaction, signifying their nonparticipation in the observed spectral changes. The interaction with Trp induces specific electron transitions within the CNS structure, eliciting the observed red-shift phenomenon. Consequently, the mechanism for Trp sensing by the CNS includes an interplay of electron transfer, interaction sites, and intramolecular alterations.

3.8.4. Detection of the Detection Limit and Quantification Limit for Trp. To unravel the minimal detectable concentration of Trp through the synthesized CNS, we performed titration studies conducted three times, spanning a range of 0−14 μg/mL. The outcome was plotted into a graph, where the mean absorbance with the wavelength revealed a red-shift in the peak due to the CNS−Trp interaction. However, with this interaction, a linear relationship also emerged when plotting the Trp concentration against absorbance at 280 nm. This trend shows the competence of CNS to discriminate minute variations in the Trp concentration, making it extremely sensitive. The quantitative assessment of the detection limit and the quantification limit followed the principles of $3\sigma/S$ and $10\sigma/S$, respectively. Here "σ" was the calculated standard deviation of blank CNS and "S" was the slope determined from a graph plotted as A/A_0 vs concentration of Trp (Figure S6). The limit of detection reached a remarkably low value of 4.510×10^{-3} μg/mL and the limit of quantification of 1.50×10^{-2} μg/mL. This quantification limit indicates that the synthesized CNSs are capable of reliably detecting such low levels of Trp with reproducibility. Additionally, the detection limit ensures the remarkable ability to detect ultralow levels of Trp concentration. Notably, this value significantly falls in the range of recommended Trp levels in biological samples.[35] Hence, the synthesized CNS can be a potential tool to detect Trp levels with great sensitivity.

3.9. Application Studies of CNS as the Cu^{2+} Sensor. Unveiling the practical utility of the synthesized CNS, our investigation extended to diverse water samples for the

https://doi.org/10.1021/acsomega.3c07544
ACS Omega 2024, 9, 4555−4571

assessment of CNS's potential as a Cu^{2+} sensor. This exploration provides an in-depth analysis of site-specific detection within the complex array and proves CNS's ability to withstand competitive ions. Furthermore, we also performed a filter paper-based test, to understand how CNS's fluorescence responds to Cu^{2+} when bound to this substrate.

3.9.1. Real Water Samples Analysis (Tap Water, Lake Water, and Distilled Water). With the above results, the synthesized CNS emerges as a credible contender for Cu^{2+} detection in various water samples. In the intended CNS−Cu^{2+} calibration curve, which spans an optimal range of 0−40 μg/mL (Figure 10), we worked to assess the CNS's performance in real water scenarios. The synthesized CNS's capabilities were tested across diverse water samples, which include tap water, lake water, and distilled water. Lake water, tap water, and distilled water were obtained from Sukhna Lake (Chandigarh, India), Sector 39 (Chandigarh, India), and CSIR-IMTECH (Chandigarh), respectively. To unravel the CNS's ability, these water samples were intentionally spiked with Cu^{2+} ions. The analysis was performed by the use of the proposed spectroscopic method, a robust approach showcased in the prior literature.[75−80] The resultant data, as presented in Table 3, provide confirmation of the synthesized analytical utility of CNS in quantifying Cu^{2+} within the authentic water spectrum. The recovery (%) values closely aligned with actual values and the calculated RSD value (%), affirming CNS's performance. The minimal divergence of recovery values from actual values shows the precision of CNS's quantification abilities. Additionally, the justifiable RSD value shows good reproducibility and repeatability. Hence, this ensures that the CNS can be used in real water sample analysis.

Table 3. Determination of Cu^{2+} in Analyzing Real Water Samples of Lake Water, Tap Water, and Distilled Water

sample	Cu^{2+} added (μg/mL)	Cu^{2+} found (μg/mL)	recovery (%)	RSD[a] (%)
lake water	10	10.09328798	100.0093	0.656583
tap water	10	10.23452915	100.0235	1.63915
distilled water	10	10.11861024	100.0119	0.833756

[a]Individual measurement is considered.

3.9.2. Filter Paper-Based Analysis. To determine the versatility of the CNS as a sensor, we performed a filter paper-based test. The standard protocol for filter paper-based analysis was followed to examine the viability of CNS.[27,34] Adhering to well-established protocols, we used filter paper, i.e., Whatman cellulose nitrate paper of an approximate size of 2 μm, which was cut into a circular disc of 4 cm diameter. This is done to examine the on-site detection potential of CNS. Further, executing the investigation, 1 paper disc was immersed in the sensor i.e., CNS solution and another in the CNS sensor containing Cu^{2+} in it for 15 min. It was then exposed to drying in an airflow. The changes were observed under well-illuminated UV light. On observation, a significant quenching effect was detected by the treatment of Cu^{2+} ions as shown in Figure 14. Consequently, this substantiates the use of synthesized CNS for the reliable on-site detection of Cu^{2+} ions. This reaffirms the practical utility and on-site detection capability of the synthesized CNS.

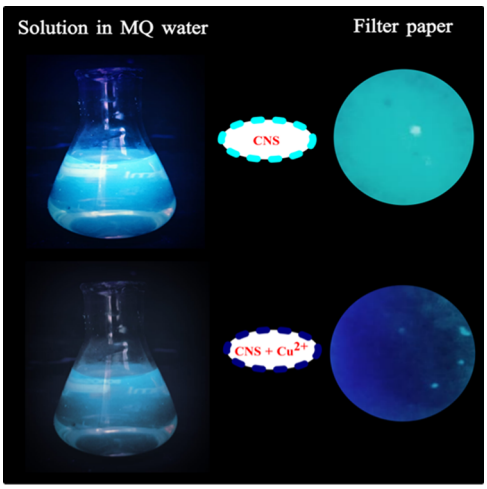

Figure 14. Clicked photograph of a filter paper-based test in UV light.

4. CONCLUSIONS

We have devised a facile CNS-based sensor via banana peels by a process through straightforward steps including banana peel grinding, pH adjustment to 3 via acetic acid, exposure to 180 °C for 15 min, and the subsequent cooling, filtration, and purification. Further, unanticipated results emerged with our study on the effect of pH on the presynthesis of CNS. Neutral pH yielded heterogeneous nanoparticles, while basic pH rendered larger, cubical-shaped monodisperse particles, which were the product of aggregation. Remarkably, the acidic pH yielded optimal results, providing monodisperse, prefunctionalized CNS with an average size of 35 nm, high solubility, and spherical morphology, herein, termed CNS. These CNS exhibited pronounced fluorescence quenching (peak at 430 nm) upon Cu^{2+} ion interaction, coupled with discernible red-shift and amplified peaks at 282 nm in UV spectra. The synthesized CNS serves as an effective 'turn-off' fluorescence sensor for Cu^{2+} ions. The quenching mechanisms through fluorescence titration, Stern−Volmer plots, and lifetime studies inferred the CHEQ (chelation enhance quenching) mechanism and static quenching on interaction of Cu^{2+} with CNS. Moreover, our synthesized CNS demonstrated the capability to sensitively detect Trp amino acid, evoking a red-shift in UV spectra accompanied by peak enhancement at 282 nm. However, with the Trp amino acid there was no significant change in the fluorescence spectra underscoring the non-involvement of the fluorophore moiety in the formation of the CNS−Trp complex. Practicality was undermined through real water sample analysis encompassing lake, tap, and distilled water. Alongside this, an investigation of the CNS−Cu^{2+} interaction via a filter paper-based approach provides promising results with on-site detection of Cu^{2+} ions. In summary, our work propounds a facile yet robust route for CNS synthesis and CNS-based sensing of Cu^{2+} ions and Trp amino acids with great practical applicability.

■ ASSOCIATED CONTENT

Supporting Information

The Supporting Information is available free of charge at https://pubs.acs.org/doi/10.1021/acsomega.3c07544.

Mechanism table specifying the process of optimization of the synthesis time. Spectral comparison of nanoparticles with acid, basic, and neutral as presynthesis

https://doi.org/10.1021/acsomega.3c07544
ACS Omega 2024, 9, 4555−4571

conditions. UV−visible spectra and fluorescence spectra of the compound formed keeping a hold time of 2 min. Graph obtained from a microwave synthesizer specifying parameters like temperature, pressure, hold time, and power. Stern−Volmer plot for CNS with Cu^{2+} and CNS with Trp amino acid. Concentration-based fluorescence and UV−visible spectra of CNS with Cu^{2+} ion (PDF)

AUTHOR INFORMATION

Corresponding Author

Raman Parkesh − *CSIR-Institute of Microbial Technology, Chandigarh 160036, India;* orcid.org/0000-0003-4096-654X; Email: rparkesh@imtech.res.in

Author

Tavishi Chopra − *CSIR-Institute of Microbial Technology, Chandigarh 160036, India; Academy of Scientific and Innovative Research (AcSIR), Ghaziabad 201002 Uttar Pradesh, India*

Complete contact information is available at: https://pubs.acs.org/10.1021/acsomega.3c07544

Notes

The authors declare no competing financial interest.

ACKNOWLEDGMENTS

The support received from CSIR-IMTECH is highly acknowledged. T.C. is grateful to the Academy of Scientific and Innovative Research (AcSIR), Ghaziabad, Uttar Pradesh, for providing financial support as a Senior Research Fellowship. The authors thank SERB for funding (Sanction Order Number CRG/2022/003805). The authors are also thankful to Dr. Sumit Chopra of GNA University, Phagwara, Punjab, for his guidance and assistance in validating our ideas and results. Additionally, we would like to express our appreciation to ChatGPT for assisting in identifying and correcting grammatical errors in our writing.

REFERENCES

(1) Britannica, The Editors of Encyclopaedia. "canistel". Encyclopedia Britannica 2018 https://www.britannica.com/plant/canistel (accessed 7 June, 2023).

(2) Hashem, A. H.; Saied, E.; Hasanin, M. S. Green and Ecofriendly Bio-Removal of Methylene Blue Dye from Aqueous Solution Using Biologically Activated Banana Peel Waste. *Sustainable Chem. Pharm.* **2020**, *18*, No. 100333, DOI: 10.1016/j.scp.2020.100333.

(3) Acevedo, S. A.; Díaz Carrillo, Á. J.; Flórez-López, E.; Grande-Tovar, C. D. Recovery of Banana Waste-Loss from Production and Processing: A Contribution to a Circular Economy. *Molecules* **2021**, *26*, No. 5282, DOI: 10.3390/molecules26175282.

(4) Azieyanti, N. A.; Amirul, A.; Othman, S. Z.; Misran, H. Mechanical and Morphology Studies of Bioplastic-Based Banana Peels. *J. Phys.: Conf. Ser.* **2020**, *1529*, No. 032091, DOI: 10.1088/1742-6596/1529/3/032091.

(5) Oberoi, H. S.; Vadlani, P. V.; Saida, L.; Bansal, S.; Hughes, J. D. Ethanol Production from Banana Peels Using Statistically Optimized Simultaneous Saccharification and Fermentation Process. *Waste Manage.* **2011**, *31* (7), 1576−1584.

(6) Hussein, H. S.; Shaarawy, H. H.; Hussien, N. H.; Hawash, S. I. Preparation of Nano-Fertilizer Blend from Banana Peels. *Bull. Natl. Res. Cent.* **2019**, *43* (1), No. 26, DOI: 10.1186/s42269-019-0058-1.

(7) Ray, S. C.; Saha, A.; Jana, N. R.; Sarkar, R. Fluorescent Carbon Nanoparticles: Synthesis, Characterization, and Bioimaging Application. *J. Phys. Chem. C* **2009**, *113* (43), 18546−18551.

(8) Chng, K. Z.; Tan, J. K. S.; Park, S.; Lim, J.; Chua, D. X. W.; Le, Q.; Fang, J.; Ouyang, J.; Yap, C. H.; Tien, S. L.; Leo, H. L.; Kim, S. Rapid One-Step in Situ Synthesis of Carbon Nanoparticles with Cellulosic Paper for Biosensing. *Sens. Actuators, B* **2021**, *339*, No. 129849, DOI: 10.1016/j.snb.2021.129849.

(9) Kotia, A.; Yadav, A.; Raj, T. R.; Keischgens, M. G.; Rathore, H.; Sarris, I. E. Carbon Nanoparticles as Sources for a Cost-Effective Water Purification Method: A Comprehensive Review. *Fluids* **2020**, *5*, No. 230, DOI: 10.3390/fluids5040230.

(10) Gisbert-Garzarán, M.; Berkmann, J. C.; Giasafaki, D.; Lozano, D.; Spyrou, K.; Manzano, M.; Steriotis, T.; Duda, G. N.; Schmidt-Bleek, K.; Charalambopoulou, G.; Vallet-Regí, M. Engineered pH-Responsive Mesoporous Carbon Nanoparticles for Drug Delivery. *ACS Appl. Mater. Interfaces* **2020**, *12* (13), 14946−14957.

(11) Nieto-Márquez, A.; Romero, R.; Romero, A.; Valverde, J. L. Carbon Nanospheres: Synthesis, Physicochemical Properties and Applications. *J. Mater. Chem.* **2011**, *21*, 1664−1672, DOI: 10.1039/C0JM01350A.

(12) Chaudhary, N.; Gupta, P. K.; Eremin, S.; Solanki, P. R. One-Step Green Approach to Synthesize Highly Fluorescent Carbon Quantum Dots from Banana Juice for Selective Detection of Copper Ions. *J. Environ. Chem. Eng.* **2020**, *8* (3), No. 103720, DOI: 10.1016/j.jece.2020.103720.

(13) Das, P.; Ganguly, S.; Bose, M.; Mondal, S.; Das, A. K.; Banerjee, S.; Das, N. C. A Simplistic Approach to Green Future with Eco-Friendly Luminescent Carbon Dots and Their Application to Fluorescent Nano-Sensor "turn-Off" Probe for Selective Sensing of Copper Ions. *Mater. Sci. Eng., C* **2017**, *75*, 1456−1464.

(14) Araya, M.; Olivares, M.; Pizarro, F. Copper in Human Health. *Int. J. Environ. Health* **2007**, *1* (4), 608−620.

(15) Atchudan, R.; Edison, T. N. J. I.; Lee, Y. R. Nitrogen-Doped Carbon Dots Originating from Unripe Peach for Fluorescent Bioimaging and Electrocatalytic Oxygen Reduction Reaction. *J. Colloid Interface Sci.* **2016**, *482*, 8−18, DOI: 10.1016/j.jcis.2016.07.058.

(16) Savonije, K.; Weaver, D. F. The Role of Tryptophan Metabolism in Alzheimer's Disease. *Brain Sci.* **2023**, *13*, No. 292, DOI: 10.3390/brainsci13020292.

(17) Van Der Goot, A. T.; Zhu, W.; Vázquez-Manrique, R. P.; Seinstra, R. I.; Dettmer, K.; Michels, H.; Farina, F.; Krijnen, J.; Melki, R.; Buijsman, R. C.; Silva, M. R.; Thijssen, K. L.; Kema, I. P.; Neri, C.; Oefner, P. J.; Nollen, E. A. A. Delaying Aging and the Aging-Associated Decline in Protein Homeostasis by Inhibition of Tryptophan Degradation. *Proc. Natl. Acad. Sci. U.S.A.* **2012**, *109* (37), 14912−14917.

(18) Verdile, G.; Fuller, S.; Atwood, C. S.; Laws, S. M.; Gandy, S. E.; Martins, R. N. The Role of Beta Amyloid in Alzheimer's Disease: Still a Cause of Everything or the Only One Who Got Caught? *Pharmacol. Res.* **2004**, *50* (4), 397−409.

(19) Goldsworthy, M. R.; Vallence, A. M. The Role of β-Amyloid in Alzheimer's Disease-Related Neurodegeneration. *J. Neurosci.* **2013**, *33*, 12910−12911.

(20) Kałużna-Czaplińska, J.; Gątarek, P.; Chirumbolo, S.; Chartrand, M. S.; Bjørklund, G. How Important Is Tryptophan in Human Health? *Crit. Rev. Food Sci. Nutr.* **2019**, *59*, 72−88.

(21) Nayak, B. N.; Singh, R. B.; Buttar, H. S.Biochemical and Dietary Functions of Tryptophan and Its Metabolites in Human Health. In *Functional Foods and Nutraceuticals in Metabolic and Non-communicable Diseases*; Elsevier Inc., 2022; pp 783−798.

(22) Wei, T. B.; Chen, J. F.; Cheng, X. Bin.; Li, H.; Han, B. B.; Zhang, Y. M.; Yao, H.; Lin, Q. A Novel Functionalized pillar[5]arene-Based Selective Amino Acid Sensor for L-Tryptophan. *Org. Chem. Front.* **2017**, *4* (2), 210−213.

(23) Khoshnevisan, K.; Torabi, F.; Baharifar, H.; Sajjadi-Jazi, S. M.; Afjeh, M. S.; Faridbod, F.; Larijani, B.; Khorramizadeh, M. R. Determination of the Biomarker L-Tryptophan Level in Diabetic and Normal Human Serum Based on an Electrochemical Sensing Method Using Reduced Graphene Oxide/gold nanoparticles/18-Crown-6. *Anal. Bioanal. Chem.* **2020**, *412* (15), 3615−3627.

(24) Sudar-Milovanovic, E.; Gluvic, Z.; Obradovic, M.; Zaric, B.; Isenovic, E. R. Tryptophan Metabolism in Atherosclerosis and Diabetes. *Curr. Med. Chem.* **2022**, *29* (1), 99−113.
(25) Wang, T.; Li, Y.; Shen, F.; Ren, J.; Yu, X. Isomeric Effect of Solvents on a Sugar-Based Supergelator with Self-Healing Ability. *Appl. Surf. Sci.* **2020**, *513*, No. 145814, DOI: 10.1016/j.apsusc.2020.145814.
(26) Mahendar, C.; Kumar, Y.; Dixit, M. K.; Dubey, M. An Li +-Enriched Co^{2+}-Induced Metallogel: A Study on Thixotropic Rheological Behaviour and Conductance. *Soft Matter* **2020**, *16* (14), 3436−3442.
(27) Sasan, S.; Chopra, T.; Gupta, A.; Tsering, D.; Kapoor, K. K.; Parkesh, R. Fluorescence "turn-Off" and Colorimetric Sensor for Fe^{2+}, Fe3+, and Cu^{2+}Ions Based on a 2,5,7-Triarylimidazopyridine Scaffold. *ACS Omega* **2022**, *7* (13), 11114−11125.
(28) Velapoldi, R. A.; Tønnesen, H. H. Corrected Emission Spectra and Quantum Yields for a Series of Fluorescent Compounds in the Visible Spectral Region. *J. Fluoresc.* **2004**, *14* (4), 465−472.
(29) Williams, A. T. R.; Winfield, S. A.; Miller, J. N. Relative Fluorescence Quantum Yields Using a Computer-Controlled Luminescence Spectrometer. *Analyst* **1983**, *108* (1290), 1067−1071.
(30) Shrivastava, A.; Gupta, V. Methods for the Determination of Limit of Detection and Limit of Quantitation of the Analytical Methods. *Chronicles Young Sci.* **2011**, *2* (1), 21.
(31) Beevi, K. R.; Fathima, A. R. S.; Fathima, A. I. T.; Thameemunisa, N.; Noorjahan, C. M.; Deepika, T. Bioplastic Synthesis Using Banana Peels and Potato Starch and Characterization. *Int. J. Sci. Technol. Res.* **2020**, *9* (1), 1809−1814.
(32) Tormena, R. P. I.; Rosa, E. V.; de Oliveira Mota, B. F.; Chaker, J. A.; Fagg, C. W.; Freire, D. O.; Martins, P. M.; Rodrigues da Silva, I. C.; Sousa, M. H. Evaluation of the Antimicrobial Activity of Silver Nanoparticles Obtained by Microwave-Assisted Green Synthesis usingHandroanthus impetiginosus(Mart. Ex DC.) Mattos Underbark Extract. *RSC Adv.* **2020**, *10* (35), 20676−20681.
(33) Nguyen, T. N.; Le, P. A.; Phung, V. B. T. Facile Green Synthesis of Carbon Quantum Dots and Biomass-Derived Activated Carbon from Banana Peels: Synthesis and Investigation. *Biomass Convers. Biorefin.* **2022**, *12* (7), 2407−2416.
(34) Sabet, M.; Mahdavi, K. Green Synthesis of High Photoluminescence Nitrogen-Doped Carbon Quantum Dots from Grass via a Simple Hydrothermal Method for Removing Organic and Inorganic Water Pollutions. *Appl. Surf. Sci.* **2019**, *463*, 283−291.
(35) Vikneswaran, R.; Ramesh, S.; Yahya, R. Green Synthesized Carbon Nanodots as a Fluorescent Probe for Selective and Sensitive Detection of iron(III) Ions. *Mater. Lett.* **2014**, *136*, 179−182.
(36) Padam, B. S.; Tin, H. S.; Chye, F. Y.; Abdullah, M. I. Banana by-Products: An under-Utilized Renewable Food Biomass with Great Potential. *J. Food Sci. Technol.* **2014**, *51*, 3527−3545.
(37) Hussain, S. A.; Ali, S.; Islam, Z. U.; Khan, M. Low-Temperature Synthesis of Graphite Flakes and Carbon-Based Nanomaterials from Banana Peels Using Hydrothermal Process for Photoelectrochemical Water-Splitting. *Physica E* **2022**, *141*, No. 115231, DOI: 10.1016/j.physe.2022.115231.
(38) Jeskey, J.; Chen, Y.; Kim, S.; Xia, Y. EDTA-Assisted Synthesis of Nitrogen-Doped Carbon Nanospheres with Uniform Sizes for Photonic and Electrocatalytic Applications. *Chem. Mater.* **2023**, *35*, 3024−3032, DOI: 10.1021/acs.chemmater.3c00341.
(39) Vadia, F. Y.; Ghosh, S.; Mehta, V. N.; Jha, S.; Malek, N. I.; Park, T. J.; Kailasa, S. K. Fluorescence "Turn OFF-ON" Detection of Fe3+ and Propiconazole Pesticide Using Blue Emissive Carbon Dots from Lemon Peel. *Food Chem.* **2023**, *428*, No. 136796, DOI: 10.1016/j.foodchem.2023.136796.
(40) Li, D. Y.; Wang, S. P.; Azad, F.; Su, S. C. Single-Step Synthesis of Polychromatic Carbon Quantum Dots for Macroscopic Detection of Hg^{2+}. *Ecotoxicol. Environ. Saf.* **2020**, *190*, No. 110141, DOI: 10.1016/j.ecoenv.2019.110141.
(41) Atchudan, R.; Edison, T. N. J. I.; Aseer, K. R.; Perumal, S.; Lee, Y. R. Hydrothermal Conversion of Magnolia Liliiflora into Nitrogen-Doped Carbon Dots as an Effective Turn-off Fluorescence Sensing, Multi-Colour Cell Imaging and Fluorescent Ink. *Colloids Surf., B* **2018**, *169*, 321−328, DOI: 10.1016/j.colsurfb.2018.05.032.
(42) Mai, X. D.; Thi Kim Chi, T.; Nguyen, T. C.; Ta, V. T. Scalable Synthesis of Highly Photoluminescence Carbon Quantum Dots. *Mater. Lett.* **2020**, *268*, No. 127595, DOI: 10.1016/j.matlet.2020.127595.
(43) Ju, J.; Chen, W. Synthesis of Highly Fluorescent Nitrogen-Doped Graphene Quantum Dots for Sensitive, Label-Free Detection of Fe (III) in Aqueous Media. *Biosens. Bioelectron.* **2014**, *58*, 219−225, DOI: 10.1016/j.bios.2014.02.061.
(44) Atchudan, R.; Muthuchamy, N.; Edison, T. N. J. I.; Perumal, S.; Vinodh, R.; Park, K. H.; Lee, Y. R. An Ultrasensitive Photoelectrochemical Biosensor for Glucose Based on Bio-Derived Nitrogen-Doped Carbon Sheets Wrapped Titanium Dioxide Nanoparticles. *Biosens. Bioelectron.* **2019**, *126*, 160−169, DOI: 10.1016/j.bios.2018.10.049.
(45) Pu, Z. F.; Wen, Q. L.; Yang, Y. J.; Cui, X. M.; Ling, J.; Liu, P.; Cao, Q. E. Fluorescent Carbon Quantum Dots Synthesized Using Phenylalanine and Citric Acid for Selective Detection of Fe3+ Ions. *Spectrochim. Acta, Part A* **2020**, *229*, No. 117944, DOI: 10.1016/j.saa.2019.117944.
(46) Xiong, G.; Pal, U.; Serrano, J. G.; Ucer, K. B.; Williams, R. T. Photoluminescence and FTIR Study of ZnO Nanoparticles: The Impurity and Defect Perspective. *Phys. Status Solidi C* **2006**, *3*, 3577−3581.
(47) Ali, H. R. H.; Hassan, A. I.; Hassan, Y. F.; El-Wekil, M. M. Development of Dual Function Polyamine-Functionalized Carbon Dots Derived from One Step Green Synthesis for Quantitation of Cu^{2+} and S2− Ions in Complicated Matrices with High Selectivity. *Anal. Bioanal. Chem.* **2020**, *412* (6), 1353−1363.
(48) Atchudan, R.; Edison, T. N. J. I.; Shanmugam, M.; Perumal, S.; Somanathan, T.; Lee, Y. R. Sustainable Synthesis of Carbon Quantum Dots from Banana Peel Waste Using Hydrothermal Process for in Vivo Bioimaging. *Physica E* **2021**, *126*, No. 114417, DOI: 10.1016/j.physe.2020.114417.
(49) Tan, X. W.; Romainor, A. N. B.; Chin, S. F.; Ng, S. M. Carbon Dots Production via Pyrolysis of Sago Waste as Potential Probe for Metal Ions Sensing. *J. Anal. Appl. Pyrolysis* **2014**, *105*, 157−165.
(50) Li, L.; Zhang, R.; Lu, C.; Sun, J.; Wang, L.; Qu, B.; Li, T.; Liu, Y.; Li, S. In Situ Synthesis of NIR-Light Emitting Carbon Dots Derived from Spinach for Bio-Imaging Applications. *J. Mater. Chem. B* **2017**, *5* (35), 7328−7334.
(51) Liu, L.; Gong, H.; Li, D.; Zhao, L. Synthesis of Carbon Dots from Pear Juice for Fluorescence Detection of Cu $^{2+}$ Ion in Water. *J. Nanosci. Nanotechnol.* **2018**, *18* (8), 5327−5332.
(52) Liu, G.; Li, B.; Liu, Y.; Feng, Y.; Jia, D.; Zhou, Y. Rapid and High Yield Synthesis of Carbon Dots with Chelating Ability Derived from Acrylamide/chitosan for Selective Detection of Ferrous Ions. *Appl. Surf. Sci.* **2019**, *487*, 1167−1175.
(53) Atchudan, R.; Edison, T. N. J. I.; Perumal, S.; Muthuchamy, N.; Lee, Y. R. Hydrophilic Nitrogen-Doped Carbon Dots from Biowaste Using Dwarf Banana Peel for Environmental and Biological Applications. *Fuel* **2020**, *275*, No. 117821, DOI: 10.1016/j.fuel.2020.117821.
(54) Liu, Z.; Jin, W.; Wang, F.; Li, T.; Nie, J.; Xiao, W.; Zhang, Q.; Zhang, Y. Ratiometric Fluorescent Sensing of Pb^{2+} and Hg^{2+} with Two Types of Carbon Dot Nanohybrids Synthesized from the Same Biomass. *Sens. Actuators, B* **2019**, *296*, No. 126698, DOI: 10.1016/j.snb.2019.126698.
(55) Qi, H.; Teng, M.; Liu, M.; Liu, S.; Li, J.; Yu, H.; Teng, C.; Huang, Z.; Liu, H.; Shao, Q.; Umar, A.; Ding, T.; Gao, Q.; Guo, Z. Biomass-Derived Nitrogen-Doped Carbon Quantum Dots: Highly Selective Fluorescent Probe for Detecting Fe3+ Ions and Tetracyclines. *J. Colloid Interface Sci.* **2019**, *539*, 332−341.
(56) Atchudan, R.; Edison, T. N. J. I.; Lee, Y. R. Nitrogen-Doped Carbon Dots Originating from Unripe Peach for Fluorescent Bioimaging and Electrocatalytic Oxygen Reduction Reaction. *J. Colloid Interface Sci.* **2016**, *482*, 8−18.

https://doi.org/10.1021/acsomega.3c07544
ACS Omega 2024, 9, 4555−4571

(57) Jiao, X. Y.; Li, L.; Qin, S.; Zhang, Y.; Huang, K.; Xu, L. The Synthesis of Fluorescent Carbon Dots from Mango Peel and Their Multiple Applications. *Colloids Surf., A* **2019**, *577*, 306−314.
(58) Sha, Y.; Lou, J.; Bai, S.; Wu, D.; Liu, B.; Ling, Y. Hydrothermal Synthesis of Nitrogen-Containing Carbon Nanodots as the High-Efficient Sensor for copper(II) Ions. *Mater. Res. Bull.* **2013**, *48* (4), 1728−1731.
(59) Lu, M.; Duan, Y.; Song, Y.; Tan, J.; Zhou, L. Green Preparation of Versatile Nitrogen-Doped Carbon Quantum Dots from Watermelon Juice for Cell Imaging, Detection of Fe3+ Ions and Cysteine, and Optical Thermometry. *J. Mol. Liq.* **2018**, *269*, 766−774.
(60) Moreira, V. A.; Toito Suarez, W.; De Oliveira Krambeck Franco, M.; Gambarra Neto, F. F. Eco-Friendly Synthesis of Cuprizone-Functionalized Luminescent Carbon Dots and Application as a Sensor for the Determination of Copper(ii) in Wastewater. *Anal. Methods* **2018**, *10* (37), 4570−4578.
(61) Sharma, S.; Umar, A.; Mehta, S. K.; Kansal, S. K. Fluorescent Spongy Carbon Nanoglobules Derived from Pineapple Juice: A Potential Sensing Probe for Specific and Selective Detection of Chromium (VI) Ions. *Ceram. Int.* **2017**, *43* (9), 7011−7019.
(62) Hoan, B. T.; Thanh, T. T.; Tam, P. D.; Trung, N. N.; Cho, S.; Pham, V. H. A Green Luminescence of Lemon Derived Carbon Quantum Dots and Their Applications for Sensing of V5+ Ions. *Mater. Sci. Eng. B* **2019**, *251*, No. 114455, DOI: 10.1016/j.mseb.2019.114455.
(63) Trampuž, M.; Žnidarič, M.; Gallou, F.; Časar, Z. Does the Red Shift in UV-Vis Spectra Really Provide a Sensing Option for Detection of N-Nitrosamines Using Metalloporphyrins? *ACS Omega* **2023**, *8*, 1154−1167, DOI: 10.1021/acsomega.2c06615.
(64) Armbruster, D. A.; Pry, T. Limit of Blank, Limit of Detection and Limit of Quantitation. *Clin. Biochem. Rev.* **2008**, *29* (Suppl 1), S49−S52.
(65) Ahmed, M.; Faisal, M.; Ihsan, A.; Naseer, M. M. Fluorescent Organic Nanoparticles (FONs) as Convenient Probes for Metal Ion Detection in Aqueous Medium. *Analyst* **2019**, *144*, 2480−2497, DOI: 10.1039/C8AN01801D.
(66) Bhaskar, R.; Sarveswari, S. Thiocarbohydrazide Based Schiff Base as a Selective Colorimetric and Fluorescent Chemosensor for Hg^{2+} with "Turn-Off" Fluorescence Responses. *ChemistrySelect* **2020**, *5*, 4050−4057, DOI: 10.1002/slct.202000652.
(67) Nagarajan, R.; Ryoo, H. I.; Vanjare, B. D.; Gyu Choi, N.; Hwan Lee, K. Novel Phenylalanine Derivative-Based Turn-off Fluorescent Chemosensor for Selective Cu^{2+} Detection in Physiological PH. *J. Photochem. Photobiol. A* **2021**, *418*, No. 113435, DOI: 10.1016/j.jphotochem.2021.113435.
(68) Lee, E.; Ju, H.; Park, I. H.; Park, S.; Ikeda, M.; Habata, Y.; Lee, S. S. Mechanistic Insights into Heavy Metal Ion Sensing by NOS2-Macrocyclic Fluorosensors: Via the Structure-Function Relationship: Influences of Fluorophores, Solvents and Anions. *Analyst* **2020**, *145*, 1667−1676, DOI: 10.1039/C9AN02466B.
(69) Maiti, K.; Mahapatra, A. K.; Gangopadhyay, A.; Maji, R.; Mondal, S.; Ali, S. S.; Das, S.; Sarkar, R.; Datta, P.; Mandal, D. Simple Bisthiocarbonohydrazone as a Sensitive, Selective, Colorimetric, and Ratiometric Fluorescent Chemosensor for Picric Acids. *ACS Omega* **2017**, *2*, 1583−1593, DOI: 10.1021/acsomega.6b00288.
(70) Mahata, S.; Bhattacharya, A.; Kumar, J. P.; Mandal, B. B.; Manivannan, V. Naked-Eye Detection of Pd^{2+} Ion Using a Highly Selective Fluorescent Heterocyclic Probe by "Turn-off" Response and in-Vitro Live Cell Imaging. *J. Photochem. Photobiol. A* **2020**, *394*, No. 112441, DOI: 10.1016/j.jphotochem.2020.112441.
(71) Vanjare, B. D.; Mahajan, P. G.; Ryoo, H. I.; Dige, N. C.; Choi, N. G.; Han, Y.; Kim, S. J.; Kim, C. H.; Lee, K. H. Novel Rhodamine Based Chemosensor for Detection of Hg^{2+}: Nanomolar Detection, Real Water Sample Analysis, and Intracellular Cell Imaging. *Sens. Actuators, B* **2021**, *330*, No. 129308, DOI: 10.1016/j.snb.2020.129308.
(72) Arslan, F. N.; Geyik, G. A.; Koran, K.; Ozen, F.; Aydin, D.; Elmas, Ş. N. K.; Gorgulu, A. O.; Yilmaz, I. Fluorescence "Turn On−Off" Sensing of Copper (II) Ions Utilizing Coumarin−Based Chemosensor: Experimental Study, Theoretical Calculation, Mineral and Drinking Water Analysis. *J. Fluoresc.* **2020**, *30* (2), 317−327.
(73) Vijila, N. S.; Athira, M.; Madanan Anju, S.; Aswathy, A. O.; Jayakrishna, J.; Sreekumar, M.; Anjali Devi, J. S.; Anjitha, B.; George, S. Folic Acid as a Bimodal Optical Probe for the Detection of TNT. *J. Fluoresc.* **2021**, *31* (4), 933−940.
(74) Olivares, M.; Uauy, R. Limits of Metabolic Tolerance to Copper and Biological Basis for Present Recommendations and Regulations. *Am. J. Clin. Nutr.* **1996**, *63*, 846S−852S, DOI: 10.1093/ajcn/63.5.846.
(75) Tian, M.; He, H.; Wang, B. B.; Wang, X.; Liu, Y.; Jiang, F. L. A Reaction-Based Turn-on Fluorescent Sensor for the Detection of Cu (II) with Excellent Sensitivity and Selectivity: Synthesis, DFT Calculations, Kinetics and Application in Real Water Samples. *Dyes Pigm.* **2019**, *165*, 383−390.
(76) Wang, P.; Xue, S.; Zhou, D.; Guo, Z.; Wang, Q.; Guo, B.; Yang, X.; Wu, J. Peptide-Based Colorimetric and Fluorescent Dual-Functional Probe for Sequential Detection of copper(II) and Cyanide Ions and Its Application in Real Water Samples, Test Strips and Living Cells. *Spectrochim. Acta, Part A* **2022**, *276*, No. 121222, DOI: 10.1016/j.saa.2022.121222.
(77) Khoshsoroor, S.; Mohammadi, A.; Khalili, B.; Mohammadi, S. A Novel Uracil-Based Chemosensor for Sequential Detection of Copper (II) and Cyanide Ions and Its Application in Real Samples. *J. Photochem. Photobiol. A* **2020**, *388*, No. 112208, DOI: 10.1016/j.jphotochem.2019.112208.
(78) Patir, K.; Gogoi, S. K. Nitrogen-Doped Carbon Dots as Fluorescence ON-OFF-ON Sensor for Parallel Detection of Copper-(ii) and Mercury(ii) Ions in Solutions as Well as in Filter Paper-Based Microfluidic Device. *Nanoscale Adv.* **2019**, *1* (2), 592−601.
(79) Sandyk, R. L-Tryptophan in Neuropsychiatry Disorders: A Review. *Int. J. Neurosci.* **1992**, *67*, 127−144.
(80) Sorrentino, P.; Iuliano, A.; Polverino, A.; Jacini, F.; Sorrentino, G. The Dark Sides of Amyloid in Alzheimer's Disease Pathogenesis. *FEBS Lett.* **2014**, *588*, 641−652.

https://doi.org/10.1021/acsomega.3c07544
ACS Omega 2024, 9, 4555−4571